Remote Sensing of Environment 307 (2024) 114163

Contents lists available at ScienceDirect

Remote Sensing of Environment

journal homepage: www.elsevier.com/locate/rse

Assessment of snow cover mapping algorithms from Landsat surface reflectance data and application to automated snowline delineation

Xiongxin Xiao [a,*], Shuang Liang [b]

[a] Institute of Geography, Oeschger Center for Climate Change Research, University of Bern, Hallerstrasse 12, 3012 Bern, Switzerland
[b] Aerospace Information Research Institute, Chinese Academy of Sciences, Beijing 100094, China

ARTICLE INFO

Edited by: Menghua Wang

Keywords:
Snow cover mapping
Snowline
Landsat-8/9
Snowline elevation
Mountain areas

ABSTRACT

The abundance of remote sensing imagery available has been extensively used for mapping snow cover extent in mountainous regions. However, previous studies have paid little attention to quantifying the uncertainties inherent in snow cover mapping algorithms when using Landsat observations, particularly in the context of delineating the snowline—a pivotal parameter for understanding the spatiotemporal dynamics of snow cover. Additionally, there is an urgent need for an automated processing approach capable of monitoring alpine snowline across expansive mountainous terrains. This study squarely addresses these gaps by primarily focusing on the precise delineation of snowline and the quantification of disparities in determining snowline elevation using eight snow cover mapping algorithms. Our approach is twofold: initially, we comprehensively assessed eight snow cover mapping algorithms using Landsat 8/9 data, contrasting their performance against high-spatial-resolution (3 m) snow observations. Subsequently, we introduced a novel snowline delineation method, termed Automated Snowline Delineation on Binary Snow Cover (ASLD-BSC). This method is designed to determine snowline on binary snow cover maps generated by these eight algorithms and was rigorously assessed across 15 catchment basins in America. The comparative analysis of the eight snow cover algorithms revealed a hierarchy of performance, with three algorithms employing multi-band decision trees exhibiting the highest proficiency in snow cover mapping. They were succeeded by four NDSI-based algorithms, with the Blue Snow Threshold algorithm ranking the lowest in terms of performance. Furthermore, our assessment demonstrated that the proposed snowline delineation method, ASLD-BSC, successfully mitigated approximately 1/3 of misclassification pixels and effectively created robust snowline patterns for each binary snow map. When scrutinizing snowline elevation, we observed striking variations in elevation differences among the eight snow cover mapping algorithms relative to the reference snowline elevation (average snowline elevation: 121 m ~ 258 m; bottom 10% snowline elevation: 253 m ~ 512 m; top 10% snowline elevation: 206 m ~ 344 m). These findings underscore the pivotal role that the quality of binary snow maps plays in determining the accuracy of snowline and snowline elevation. Importantly, this study provides a comprehensive guide for selecting appropriate snow cover mapping algorithms, facilitating effective monitoring of Landsat-based snow cover in mountainous areas.

1. Introduction

Snowpack is a highly sensitive component of the Earth system that is greatly affected by climate change. The significance of the snowpack lies in its role within this system (Barnett et al., 2005; Xiao et al., 2018). The decrease in snow accumulation has far-reaching implications, strongly impacting various aspects such as wildlife diversity, functional composition of ecosystems, winter sport tourism, energy balance, and hydroelectricity generation (Huning and AghaKouchak, 2020; Kelsey et al., 2021; Niittynen et al., 2020, 2018; Painter et al., 2010). The shifting of rain-to-snow ratio due to increased temperature indicates that a higher proportion of precipitation fall as rain rather than snow, consequently leading to a substantial reduction in streamflow (Berghuijs et al., 2014). Reduction of snowpack mass has a profound impact on food production in agricultural irrigation areas reliant on snowmelt water for irrigation, thereby negatively affecting both local population and socioeconomic conditions (Qin et al., 2022, 2020). Furthermore, the decrease in snow cover causes habitat loss for certain species inhabiting high-latitude ecosystems (Niittynen et al., 2018), indicating that considering the effects of snow cover duration becomes crucial for forecasting biodiversity

* Corresponding author.
E-mail address: xiongxin.xiao@unibe.ch (X. Xiao).

https://doi.org/10.1016/j.rse.2024.114163
Received 6 September 2023; Received in revised form 13 March 2024; Accepted 13 April 2024

patterns and effectively managing nature conservation areas.

Given the immense importance of snowpack, there is an increasing need to monitor historical and current changes in snow cover (Xiao et al., 2020), employing in-situ measurements and satellite imagery. Apart from assessing snow cover extent and snow water equivalent (or snow depth), snowline serves as a crucial parameter for characterizing spatiotemporal variations in snow cover within mountain regions. The umbrella term "snowline" encompasses various definitions depending on the application conditions: 1) In the field of atmospheric sciences, the snowline refers to the boundary between snow and rain. Precipitation below the elevation of the snowline (i.e., 0 °C isotherm elevation) is considered rainfall, while precipitation above it is classified as snowfall (Minder et al., 2011). 2) In glacial studies, the snowline corresponds to the equilibrium line of a glacier at the end of ablation season. It signifies the transition line between accumulation and ablation zones of glacier (Shea et al., 2013). The movement of the glacial snowline indicates whether the glacier is advancing (growing) or retreating (shrinking). 3) In climatic studies, the snowline represents the demarcation between snow-covered zone and snow-free zone (Wunderle et al., 2002). The permanent snowline denotes the uppermost boundary of snow-free area, above which snow cover persists year-round. It is important to note that snowline can have additional definitions in other fields, for example, meteorological and hydrological studies (Gafurov and Bárdossy, 2009; Hantel and Maurer, 2011).

In this study, the snowline serves as the delineation of snow cover extent, specifically referring to climatic snowline. Variations in snowline provide insights into the dynamics of seasonal snow cover. As a result of climatic variability, the highest snowline during late summer can recede or advance from year to year. Typically, snowlines are determined through the analysis of remote sensing images captured by cameras and satellites. The traditional interactive data processing method for snowline delineation is evidently insufficient to meet the anticipated efficiency requirements of data processing in the era of remote sensing big data. Wunderle et al. (2002) employed the neighborhood statistics method to establish a robust and reliable snowline at the watersheds scale using Advanced Very High Resolution Radiometer (AVHRR) data. This method required that localized pixels of snowline had at least one adjacent edge corresponding to a snow-free pixel. Researcher further applied this approach to extract snowline from Moderate Resolution Imaging Spectroradiometer (MODIS) data over the Tibetan plateau while also considering the removal of the influence of lake masks (Tang et al., 2014). One notable disadvantage of this method is its susceptibility to patchy snow cover extent, cloud cover, and shadows, which can lead to false snowline identification. In contrast, Parajka et al. (2010) proposed a method to determine a regional snowline by obtaining the average elevation of all snow-covered pixels and then using this threshold to assign cloud pixels as either snow-covered or snow-free. Subsequently, Krajčí et al. (2014) developed a widely accepted approach for delineating regional snowlines (RSL) from MODIS data. This method involved finding the minimum sum of snow-free pixels above a given elevation and snow-covered pixels below it to determine the regional snowline elevation (Gascoin et al., 2019). While the statistic-based RSL method has been successfully applied in numerous studies analyzing snowline variations (Hu et al., 2019; Koehler et al., 2022; Portenier et al., 2022; Wang et al., 2023), it is important to acknowledge its limitations. The RSL method assigns the same snowline elevation for all aspects within a basin, and it is only applicable to small sub-basins (Girona-Mata et al., 2019). Additionally, concerns have been raised regarding the method's ability to accurately represent the true snow cover extent (Koehler et al., 2022). Furthermore, the snowline for MODIS minimum snow cover extent can be extracted based on the frequency of snow cover per year using a threshold of 80% (Lei et al., 2012). Girona-Mata et al. (2019) developed an intriguing method that involved converting Landsat's binarized snow cover pixels into point features in ArcGIS. Through subsequent processing operations on these point features, the snowline within a sub-catchment of Langtang Valley was successfully extracted. However, the portability of this method to other data processing platforms greatly limits its application. Several studies have also investigated snowlines in glaciers by using remote sensing data to differentiate between snow and ice boundaries in order to determine glacier equilibrium lines (Li et al., 2022; Racoviteanu et al., 2019; Shea et al., 2013; Yu et al., 2022). The presence of numerous small snow patches in close proximity to the boundary of snow cover extent has posed challenges in representing snowline as a boundary of snow cover extent using remote sensing data (Gafurov and Bárdossy, 2009; Krajčí et al., 2014; Wunderle et al., 2002). Given the great large volume of remote sensing images that need to be processed for alpine snowline monitoring, there is an urgent need for an automated processing approach that can be applied over large mountain areas.

Start-of-the-art methodologies for snowline delineation typically involve an initial step of a snow cover mapping algorithm to generate a binary snow cover map, which is then used to determine snowline (Girona-Mata et al., 2019; Krajčí et al., 2014; Lei et al., 2012; Shea et al., 2013). The Normalized Difference Snow Index (NDSI) based method is commonly employed to exploit the distinct spectral characteristics of snowpack. Past studies have utilized various binary snow classification techniques in remote sensing data for snowline delineation, including NDSI-based method (Girona-Mata et al., 2019), SNOWMAP algorithm (Wang et al., 2023), K-means classification algorithm (Shea et al., 2013), and OTSU-based-NDSI method (Li et al., 2022). These approaches primarily focused on directly performing snowline delineation using one of snow cover mapping algorithms and analyzing the trends in snowline variation and elevation. However, previous studies on snowline variation have often neglected to account for the uncertainties introduced by snow cover mapping algorithms. Additionally, publications pertaining to the development of snow cover mapping algorithms have mainly compared their snow classification or snow area estimation capability (Hao et al., 2019; Rittger et al., 2013; Stillinger et al., 2023; Xiao et al., 2022, 2021; Yin et al., 2013). For instance, a study examined eleven snow cover mapping algorithms in classifying snow cover using five Landsat TM images, including automatic thresholding methods and a support vector machine method (Yin et al., 2013). The findings indicated that the OTSU-based-NDSI method achieved robust snow cover classification. Another study by Stillinger et al. (2023) evaluated the United States Geological Survey (USGS) Landsat-based fractional snow cover area (USGS Landsat fSCA) products and two spectral unmixing algorithms in 12 Landsat images, concluding that spectral-mixture methods showed promise in estimating fractional snow cover area when compared against Airborne Snow Observatory (ASO) 3 m snow depth data. Despite these advancements, few past studies have specifically illuminated the uncertainties associated with snow cover mapping algorithms when delineating snowline using Landsat snow cover maps.

The motivation behind this study is to advance the development of snow cover area estimation approaches and enhance our understanding of the observed/evident reduction in snow cover area in mountainous region over the past decades. Building upon the analysis of previous studies, this study aims to achieve the following objectives:

- To comprehensively validate and compare multiple snow cover mapping algorithms using independent ASO 3 m snow depth data.
- To develop a snowline delineation method that accurately captures snow cover extents and can be easily applied across various mountainous areas.
- To quantify the differences associated with snow cover mapping algorithms in delineating snowline and analyze their impact on determining snowline elevation.

By addressing these objectives, this study applied eight snow cover mapping algorithms on 25 Landsat-ASO image pairs to analyze the accuracy and reliability of snow cover mapping algorithms and provide insights into the influence of different snow cover mapping algorithms on snowline delineation.

2. Data sets

2.1. ASO snow depth dataset

The ASO aerial lidar data were utilized to produce high spatial resolution snow depth and snow water equivalent datasets with a spatial resolution of 3 m and 50 m, respectively (Painter et al., 2016). ASO snow depth data has been extensively employed for monitoring snow cover variations in mountainous regions, particularly for snow simulation and evaluation purposes (Brandt et al., 2020; Hedrick et al., 2018; Margulis et al., 2019; Stillinger et al., 2023). All ASO snow products mentioned are archived by the National Snow and Ice Data Center (NSIDC) and the ASO Inc. website. These datasets cover the period from 2013 to 2022 (last accessed on April 20, 2023).

Prior to the establishment of image matching pairs between Landsat and ASO snow images, we filtered all available 99 ASO snow images from NSIDC and 147 ASO snow images from ASO Inc. one by one, based on Landsat image path/row. Several selection criteria were applied: 1) each ASO snow depth image corresponds to only one Landsat image for a given date; 2) both snow-free and snow-covered pixels are present in ASO snow depth data; and 3) there is an overlap between the common area of Landsat image and ASO snow products. Following this selection process, we obtained 25 image matching pairs consisting of ASO snow depth data and Landsat data. The specific data lists can be found in Table S1 in the Supplement. Table 1 summarizes the spatial location information of these 25 image pairs.

A series of processes were implemented to convert the 3 m ASO snow depth data into the reference snow cover observations at a 30 m scale. Firstly, the 3 m ASO snow depth data underwent quality control to address the representation issue of "zero" values (Stillinger et al., 2023), encompassing fill values and snow-free class. Data cleaning of 3 m ASO snow depth data is performed as a mandatory process step to avoid a substantial number of false negative data in the validation results and prevent the creation of inaccurate snowline records (refer to Fig. S1 (right) in the Supplement; yellow arrows). In contrast, the 50 m snow depth and snow water equivalent products had been conducted through rigorous quality control. The 50 m snow depth and snow water equivalent data were employed to define the basin boundaries of the corresponding 3 m ASO snow depth observations, and its filled values were removed.

Next, snow depth values of 3 m ASO snow depth data were converted into binary snow cover values, where a snow-free classification represented snow depth <8 cm, and a snow-covered classification indicated snow depth >8 cm. Painter et al. (2016) have previously indicated that the uncertainty of 3 m ASO snow depth is lee than 8 cm in terms of root mean square errors (RMSE). These binary snow cover maps at a 3 m scale are considered the "true" ground snow measurements. Subsequently, the 3 m ASO binary maps were aggregated into fractional snow cover (FSC) maps with a 30 m resolution (Xiao et al., 2022). As our assessment experiments were focused on binary snow cover derived from Landsat images, further conversion from fractional to binarized values at a 30 m scale was necessary. Unlike a previous study (Stillinger et al., 2023) that employed a threshold of 0 for FSC to determine snow-free and snow-covered areas, we conducted sensitivity analysis experiments to select an optimal threshold for converting the aforementioned fractional values at a 30 m scale (refer to Section 4.1 for more details). In this study primarily employed 25 ASO binary snow maps (30 m) to validate the snow cover classification results derived from Landsat imagery. Subsequently, the proposed snowline delineation method was applied to these ASO maps to generate a snowline reference benchmark for comparison with the snowlines extracted from Landsat Data. It is important to note that ASO data cannot be considered immaculate snow cover observations for validation purposes, and Section 5.1 discusses the associated uncertainties.

Table 1
The summary of image matching pairs for ASO snow depth data and Landsat data (please refer to the Supplement for additional details).

ASO data source	U.S. state name	ASO flight time	Flight watershed (Site code)	Landsat Path/row
NSIDC	Colorado	2018-03-30	Gunnison-Taylor River (USCOGT)	035/033
NSIDC	Colorado	2018-03-30	Crested Butte (USCOCB)	035/033
NSIDC	California	2019-04-28	Kings Canyon (USCAKC)	041/034
NSIDC	California	2017-07-18 2018-04-23	San Joaquin South Fork (USCASF)	042/034 043/034
NSIDC	California	2018-04-23	San Joaquin Jose Willow (USCAJW)	043/034
NSIDC	California	2017-07-18	Lakes Basin (USCALB)	042/034
NSIDC	California	2016-04-01 2016-04-26 2018-04-23	Tuolumne Cherry/ Eleanor (USCATE)	043/033 042/034 043/034
ASO Inc.	Colorado	2022-04-19	Blue River	034/033
ASO Inc.	Wyoming	2022-06-11	Green River	037/030
ASO Inc.	California	2022-04-01	Feather River	044/032
ASO Inc.	California	2022-03-27	Kaweah River	041/035
ASO Inc.	California	2020-04-14 2022-05-14 2022-03-02	Kings Canyon	041/035 042/034
ASO Inc.	California	2020-05-07 2020-05-23 2022-03-01 2022-05-13	Merced River	042/034 043/034
ASO Inc.	California	2020-05-07 2020-05-23	Tuolumne River	042/034
ASO Inc.	California	2020-05-23 2020-06-08 2022-02-06	San Joaquin	042/034

2.2. Landsat-8/9 surface reflectance data

We obtained the Landsat Collection 2 Level-2 surface reflectance imageries from the USGS Earth Explorer. The selection of Landsat data was based on the data matching list for ASO snow depth data and Landsat surface reflectance data. A total of 19 Landsat tiles were selected, consisting of 15 Landsat-8 images and 4 Landsat-9 images (refer to Tables S1 and S2). These tiles were used for identifying snow-free and snow-covered areas using eight different snow cover mapping algorithms (See Section 3.1). Cloud, shadow, fill values, and water pixels were excluded based on the Quality Assessment layer generated using the Fmask 4.6 algorithm (Qiu et al., 2019; Zhu et al., 2015). Since most of study areas are located in mountainous regions, where terrain effects can impact Landsat images (Ma et al., 2021; Yin et al., 2022), a topographic correction method (Teillet et al., 1982) was applied to Landsat

images in this study (Ma et al., 2021). After preprocessing Landsat data, surface reflectance pixels with abnormal values (outside the range of 0 to 1) were masked. Additionally, potential water body pixels in Landsat images were excluded from land cover data (see Section 2.4). The processed Landsat surface reflectance pixels were then used as input for eight snow cover mapping algorithms.

2.3. ALSO AW3D30 DEM data

The AW3D30 digital elevation model (DEM) data, developed by Japan's Aerospace Exploration Agency (JAXA) (Takaku et al., 2014), was utilized in this study. AW3D30 provides global coverage with a resolution larger than most DEM data (Wei et al., 2020). The AW3D30 DEM data with a 30 m spatial resolution was employed to correct topography effects in Landsat 30 m images and determine snowline

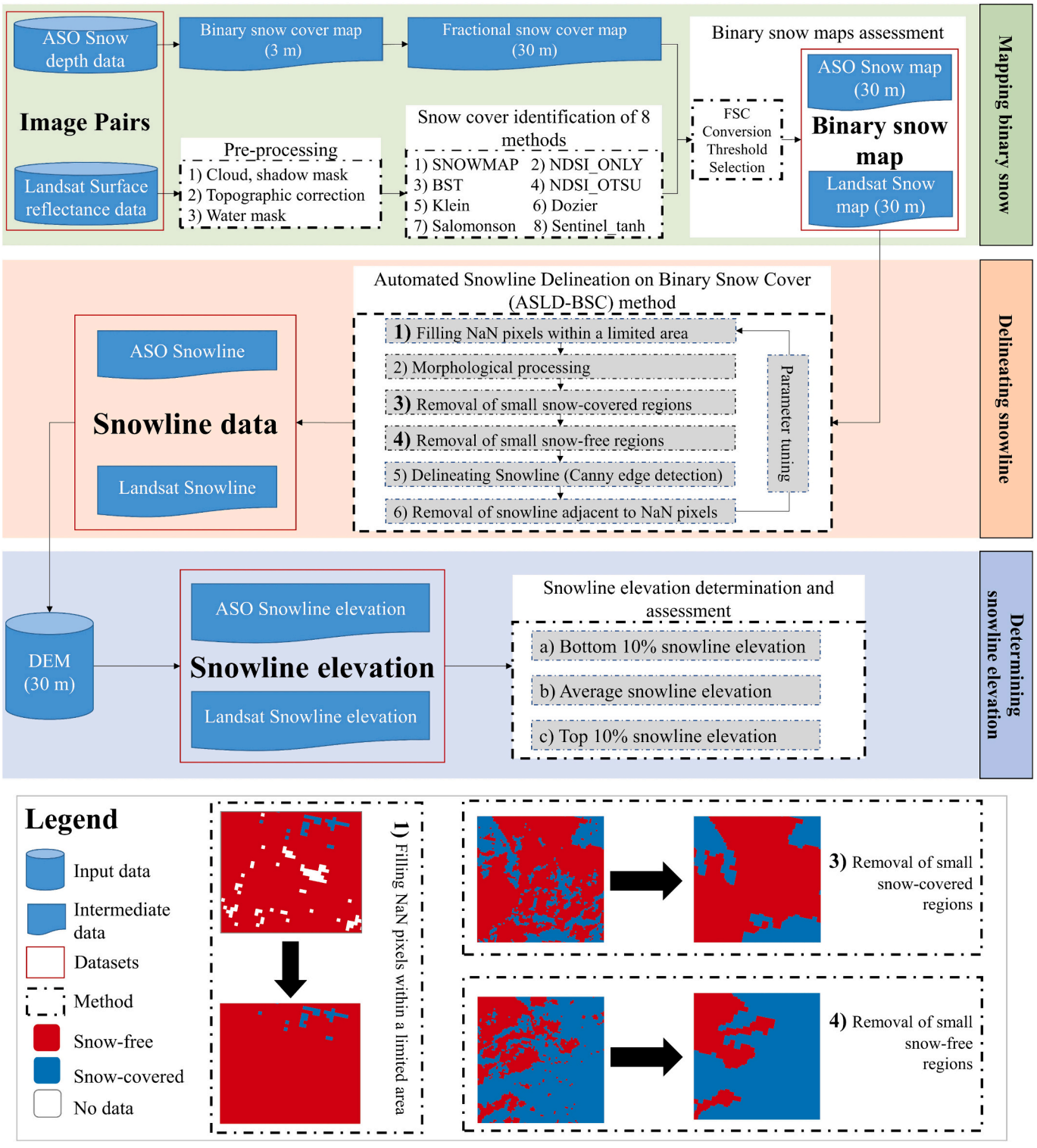

Fig. 1. Flowchart of the processing chain for mapping snow cover, delineating snowline, and determining snowline elevation. The last row represents the data processing schematic diagram for snowline delineation, indicated by 1), 3), and 4).

elevation. Slope and aspect data were derived from this DEM data using a Python program. The DEM, slope, and aspect data were used in topographic correction method for Landsat surface reflectance. Additionally, DEM data played a role in determining snowline elevation. It is important to note that the uncertainty associated with DEM data is well known (Dozier et al., 2022), and it may impact the accuracy of topographic correction for Landsat data and the determination of snowline elevation. However, the assessment of this uncertainty falls beyond the scope of this paper.

2.4. National Land Cover Database (NLCD) 2019

In this study, the NLCD 2019 land cover data at a 30 m spatial resolution was obtained for the conterminous United States. This data, described by Wickham et al. (2021), contains 17 Level-II land cover classes and 8 Level-I land cover classes. For our analysis, we reclassified this Level II classification scheme into five land cover classes: water, bare land, grassland, forest, and shrub (refer to Table S3 in the Supplement). The land cover data were cropped using Landsat images and ASO snow data at 30 m scale. The NLCD land cover data was employed for two distinct purposes. First, it served to mask water body pixels within Landsat images during preprocessing. Second, the NLCD data was leveraged to group the snow cover classification results, facilitating the assessment of snow cover mapping algorithm (seeing Section 4.1).

3. Methods

In this study, we comprehensively analyzed the mapping ability of snow cover algorithms using Landsat data for mapping binary snow cover and investigated their influence on snowline delineation. The snowline serves as an important indicator for monitoring variations in mountain snow cover and provides insights into changes in snow cover extent. Manual delineations of snowline is time-consuming and cannot keep pace with the growing number of satellite images. To address this, a highly automated delineation method was developed in this study. Fig. 1 illustrates the detailed data processing pipeline proposed for snowline delineation. The pipeline consists of three parts: mapping binary snow, delineating snowline, and determining snowline elevation. In the first part (mapping binary snow), Landsat surface reflectance data underwent a series of data pre-processing (see Section 2.2) to generate Landsat binary snow maps using various snow cover mapping methods (see Section 3.1). The conversion process from ASO 3 m snow depth data to ASO 30 m binary snow maps is described in detail in Section 2.1. The second part (delineating snowline) then involves the development of an automatic snowline delineation method using the binary snow maps from Landsat and ASO (see Section 3.2). This method is applied to image-matching pairs of Landsat data and ASO snow data to delineate snowline. The last part focuses on determining snowline elevation for different snowline maps (Section 3.3).

3.1. Snow cover mapping algorithms

Remote sensing techniques rely on the physical properties of snow, such as its high reflectivity in the visible spectrum and strong absorption in the shortwave infrared spectrum, to map snow cover. Numerous studies have utilized this characteristic to discriminate snow from other elements (Hall et al., 1995; Rittger et al., 2013; Xiao et al., 2022). In this study, we compared eight snow cover mapping approaches, namely Hall et al. (1995) (referred to as SNOWMAP), Girona-Mata et al. (2019) (referred to as NDSI_ONLY), Härer et al. (2018) (referred to as NDSI_OTSU), Thaler et al. (2023) (referred to as BST), Klein et al. (1998) (referred to as Klein), Dozier and Painter (2004) (referred to as Dozier), Salomonson and Appel (2004) (referred to as Salomonson), and Gascoin et al. (2020) (referred to as Sentinel_tanh). These eight methods were widely used for obtaining binary snow cover maps from remote sensing images. Therefore, we comprehensively analyzed their performance in mapping binary snow compared to the reference ASO binary snow map (30 m). While numerous studies have employed machine learning techniques for snow cover area estimation (Czyzowska-Wisniewski et al., 2015; Xiao et al., 2022), it's important to note that we did not undertake machine learning methods primarily due to the limited availability of co-registered ASO-Landsat image pairs suitable for raining and validating a robust ML model. Table 2 summarizes the characteristics of these eight snow cover mapping algorithms. Brief descriptions of these algorithms are provided below; detailed information can be found in corresponding literature.

3.1.1. SNOMAP

Hall et al. (1995) developed the SNOWMAP algorithm for snow cover mapping, which involves the criteria tests using NDSI (Eq. 1), Normalized Difference Vegetation Index (NDVI, Eq. 2), as well as the reflectance threshold in Near-Infrared band (NIR, 0.85 μm). This algorithm has been widely applied with Landsat images to obtain the reference snow cove observations (binary or fractional) for various snow-related studies (Dobreva and Klein, 2011; Hao et al., 2021; Xiao et al., 2022).

$$NDSI = \left(Green_{0.55\mu m} - SWIR_{1.6\mu m}\right) / \left(Green_{0.55\mu m} + SWIR_{1.6\mu m}\right) \quad (1)$$

$$NDVI = \left(NIR_{0.85\mu m} - Red_{0.66\mu m}\right) / \left(NIR_{0.85\mu m} + Red_{0.66\mu m}\right) \quad (2)$$

3.1.2. NDSI_ONLY

Previous studies generally used a statistic value as the NDSI threshold to discriminate snow cover from other surface elements. In the Himalayas region, Girona-Mata et al. (2019) applied a statistic threshold (0.45) of NDSI to identify snow-covered pixels in Landsat images. These binary snow cover maps were then used to delineate snowline. In this study, the name "NDSI_ONLY" denotes the method used in Girona-Mata et al. (2019) study.

3.1.3. NDSI_OTSU

It is challenging to determine a uniform threshold for NDSI that effectively distinguish between snow-covered and snow-free areas. This NDSI threshold varied with time and space. Therefore, some studies have utilized OTSU's method (Otsu, 1979) to obtain a dynamic threshold for NDSI in determining binary snow cover maps (Härer et al., 2018; Yin et al., 2013).In this study, we also examined the ability of this method for snow cover mapping, referred to as NDSI_OTSU. The thresholds of NDSI using the NDSI_OTSU method for 19 Landsat images used in this study are shown in the Supplement Table S2.

Table 2
Summary of the characteristics of eight snow-cover mapping methods used for Landsat in this study. Most of the methods utilize NDSI as input for snow cover mapping, except BST, which uses the reflectance of blue band (Blue: 0.48 μm). NDSI: Normalized Difference Snow Index. NDVI: Normalized Difference Vegetation Index. NIR: Near-Infrared (0.85 μm). The green band represents the reflectance in the spectral range of 0.55 μm.

Algorithm name	Involved variables	Output types (Fractional/Binary)	Reference
SNOWMAP	NDSI, NDVI, NIR	Binary (0 or 1)	Hall et al. (1995)
NDSI_ONLY	NDSI	Binary (0 or 1)	Girona-Mata et al. (2019)
NDSI_OTSU	NDSI	Binary (0 or 1)	Härer et al. (2018)
BST	Blue	Binary (0 or 1)	Thaler et al. (2023)
Klein	NDSI, NDVI, Green, NIR	Binary (0 or 1)	Klein et al. (1998)
Dozier	NDSI, NIR	Binary (0 or 1)	Dozier and Painter (2004)
Salomonson	NDSI	Fractional (0–1)	Salomonson and Appel (2004)
Sentinel_tanh	NDSI	Fractional (0–1)	Gascoin et al. (2020)

3.1.4. BST

Thaler et al. (2023) introduced an innovative method called Blue Snow Threshold (BST) algorithm, which utilizes the blue band (0.48 μm) to map snow cover. This automatic algorithm has been validated and evaluated using high-resolution satellite images from PlanetScope. In this study, we applied the BST algorithm (its codes provided by Evan A. Thaler) to Landsat images and evaluated its performance. The blue band thresholds of 19 Landsat satellite images were analyzed by the BST algorithm, and the thresholds for each image are presented in Table S2 (in the Supplement).

3.1.5. Dozier

The snow cover mapping approach of Dozier and Painter (2004) incorporates the reflectance in the NIR band and NDSI. Pixels that meet specific threshold conditions for NDSI and $NIR_{0.85\mu m}$ are classified as snow-covered, while others are considered snow-free. In this study, we refer to this approach as Dozier. The Dozier method has been used to generate one of the standard high-resolution snow observations used to validate European Space Agency (ESA) Climate Change Initiative (CCI) snow products (Ripper et al., 2019).

3.1.6. Klein

Klein et al. (1998) proposed another binary snow mapping algorithm, referred to as Klein in this study, which has been used to validate ESA CCI snow products (Ripper et al., 2019). Klein algorithm differs from above-mentioned five binary snow map algorithms as it utilizes additional variables to define decision rules (Table 2), including NDSI, NDVI, $NIR_{0.85\mu m}$, and $Green_{0.55\mu m}$.

3.1.7. Salomonson

Salomonson and Appel (2004) proposed a linear FSC estimation algorithm based on NDSI used to derive FSC area from MODIS surface reflectance data. In this study, we refer to this algorithm as Salomonson. It was previously employed to generate MODIS Version 5 standard FSC products and was also included in validating ESA CCI snow products to obtain the reference snow observations. We converted fractional values to binary values through a series of sensitive tests (see Section 4.1).

3.1.8. Sentinel_tanh

For the Sentinel-2 image (20 m), Gascoin et al. (2020) developed the Sentinel_tanh algorithm, which uses a sigmoid-shaped function for FSC estimation. This empirical algorithm was trained using NDSI and validated with various high-resolution reference observations. In this study, we directly applied this empirical function to retrieve FSC from Landsat surface reflectance data. The fractional values were converted to binary values (see Section 4.1).

3.2. Snowline delineation method

Based on the generated binary snow maps (ASO and Landsat), we developed a 6-steps automated method to delineate the snowline (Fig. 1), named automated snowline delineation on binary snow cover (ASLD-BSC), which underwent extensive testing. Please note that Fig. 1 visually represents the outcomes of these data processing steps. Here, we provide a detailed description of the data processing steps involved in this method:

The binary snow map may contain NaN pixels, where the snow-covered or snow-free areas are unclear due to various factors like cloud, shadows, and low-quality data. Therefore, the first step is to address these NaN pixels (denote no valid data) within a limited area. Initially, we tested a search window of 150 m * 150 m (5 * 5) centered on the NaN pixel. If more than half of the pixels within the search window are identified as snow-covered, the NaN pixel is assigned as snow-covered; otherwise, it is snow-free. If there are insufficient valid pixels ($< 0.5 * 5 * 5$), the search window is extended to 500 m * 500 m (17 * 17), and the same process is repeated. If there are still not enough valid pixels, no action is taken. The choice of a 500 m search window is based on the MODIS pixel size. The results of this process can be seen in Fig. 1, labeled "Filling NaN pixels within a limited area".

The second step is the "morphological processing". The binary snow map obtained from the first step may contain false positives and false negatives, indicating pixels were incorrectly identified as snow-covered or snow-free. To address these issues, we used the Python library to perform a series of morphological options as a preprocessing step for binary snow maps (Bishop-Taylor et al., 2021). Specifically, we applied morphological closing using a 3 * 3 structuring kernel to address small gaps in snow-covered or snow-free pixels. This was followed by a morphological opening with a structure size of 3×3 pixels to eliminate thin linear features.

In steps three and four of this procedure, we refined the binary snow maps by eliminating small snow-covered regions and small snow-free regions that the area is less than 0.25 km^2, equivalent to a MODIS pixel area. Although there were small snow-covered patches in the large snow-free regions, we removed them to avoid inaccuracies in snowline delineation that would not reflect the true patterns of snowline. We replaced these small snow-covered patches with snow-free labels to ensure the complete removal of small patches. Similarly, we carried out the same operation on small snow-free patches in large snow-covered regions.

The fifth is to acquire snowline images for each binary snow map. We employed the Canny detector, an edge detector available in the Python cv2 library, with a minimum threshold = 50 and a maximum threshold = 150, to define snowline (Lai et al., 2020; Wang et al., 2022). The parameters used in this snowline delineation method were determined through multiple experimental tests. In theory, snowline presents the boundary of snow cover extent, and the snowline delineation accuracy depends on a visual inspection to verify if snowline coincides with the boundary of binary snow map created in the fourth step.

As such, the final step involves removing the snowline records around NaN pixels (3 pixels) of the binary snow cover created in the fourth step. Despite processing the binary snow map in the fourth step, some pixels with NaN values still existed. Consequently, these NaN pixels result in false snowline boundaries in the snowline image obtained in the fifth step. A post-processing operation was necessary to eliminate these false snowlines.

We fine-tuned the parameters of ASLD-BSC method on one binary snow map and then transferred these parameters to another binary snow map. We visually inspected the snowline location relative to the boundary of snow cover extent, along with saving the parameter combinations. Whenever we detected errors in some binary snow map images, we adjusted the parameters combinations and tested it on various binary snow maps. After more than 400 iteration tests, we established current parameters combinations that perform well across all binary snow maps. The snowline delineation procedure output for each image is aligned with the boundary location of snow cover extent. However, because of the presence of NaN pixels, the final snowline image only depicts a portion of snowline location.

3.3. Evaluation measures for comparing snow cover mapping algorithms

This study aims to evaluate the ability of different snow cover mapping algorithms on Landsat images using high-resolution snow observations as a benchmark. To achieve this, a series of sensitivity tests were conducted to determine a suitable threshold of FSC for converting fractional values to binary values. The study tested thresholds of 0, 0.1, 0.3, and 0.5, all of which had been previously used in snow cover area-related research (Rittger et al., 2013; Stillinger et al., 2023; Xiao et al., 2022). Ultimately, a threshold of 0.3 was chosen to convert FSC to binary snow (see Section 4.1 for details).

We employed 25 reference ASO snow cover maps (30 m) to validate the Landsat snow cover maps generated by eight snow cover mapping algorithms on a pixel-by-pixel basis. These matching pixels are

categorized into four groups by calculating a confusion matrix, including true positive (TP), false positive (FP), true negative (TN), and false negative (FN). Furthermore, to assess the performance of snow cover mappings, we employed six accuracy metrics (Xiao et al., 2022, 2021), 1) Overall Accuracy (OA) represents the total proportion of both snow-covered and snow-free pixels correctly classified, 2) Precision, highlighting commission errors (CE), reflects the proportion of predicted snow-covered pixels that are truly snow-covered, 3) Recall, highlighting omission errors (OE), measures the proportion of actual snow-covered pixels that are correctly identified, 4) Specificity represents the proportion of correctly classified snow-free pixels, 5) F1_score is a harmonic mean between precision and recall, offering a balanced view of the model's performance in binary classification, and 6) Cohen's Kappa coefficient assesses the agreement between the snow cover products retrieved by the algorithms and ground truth measurements. The comparison analysis only used pixels considered valid by all eight snow cover mapping algorithms to ensure a fair comparison.

Moreover, to investigate the impacts of snow cover mapping algorithm on snowline delineation, OE and CE were also calculated using the confusion matrix maps (TP, FP, TN, and FN; Fig. 7) (Xiao et al., 2021) under two conditions, i.e., above and below snowline (refer to Section 4.2). This analysis is in favor of comprehending the uncertainty in snowline delineation and snowline elevation determination arising from snow cover misclassification. Subsequently, the difference in snowline elevation derived from eight snow cover mapping algorithms was analyzed using three metrics, including bottom 10% snowline elevation, average snowline elevation, and top 10% snowline elevation (Fig. 1; Section 4.4).

4. Results

This study represents the most comprehensive assessment of eight snow cover mapping algorithms for Landsat surface reflectance data to date. The performance of these algorithms was evaluated against reference ASO 30-m binary snow cover maps using seven accuracy metrics. Additionally, we examined the impacts of snow cover mapping algorithms on snowline delineation, as assessed by commission error and omission relative to snowline. Finally, we analyzed the difference of the snowline derived from eight snow cover mapping algorithms against the reference ASO snowline using three snowline elevation metrics.

4.1. Assessment of snow cover mapping accuracy

In this study, we obtained the fractional values in snow cover map (30 m) only through three approaches, namely ASO_Snow, Sentinel_tanh, and Salomonson. Therefore, a series of sensitive tests were conducted to determine an optimal threshold for converting fractional values to binary values, using four FSC thresholds widely used (0, 0.1,

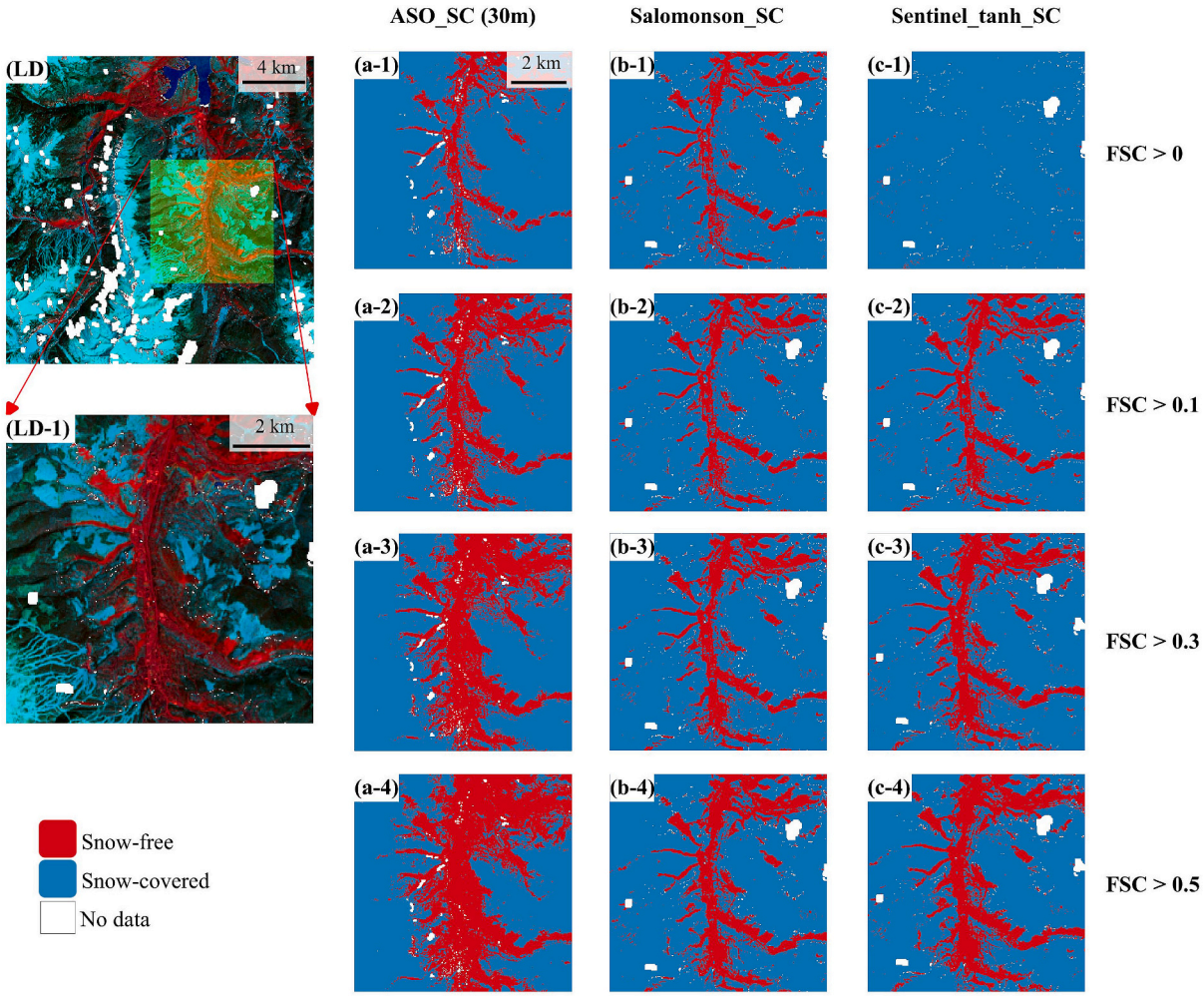

Fig. 2. The spatial patterns of binary snow cover map with different thresholds of fractional snow cover (FSC > 0, 0.1, 0.3, 0.5) on Landsat and ASO image pair (LC08_034033_20220419-ASO_BlueRiver_2022Apr19). Two Landsat-8 false-color images (SWIR1/NIR/RED), named LD and LD-1, are in the left-hand first panel. ASO_SC, Salomonson_SC, and Sentinel_tanh_SC panels are the snow cover distributions of the LD-1 area. White in all sub-images denotes no data due to the cloud, no valid data. (For interpretation of the references to color in this figure legend, the reader is referred to the web version of this article.)

0.3, 0.5; see Figs. 2 and 3).

Figure 2 presents an example of the visual snow cover map for each threshold. The snow-free area in the binary snow cover map for all three algorithms increased with the increase in FSC threshold. In the case where FSC > 0, we observed inaccurate characterization of snow cover distribution in a small region (LD-1 of Landsat scene LC08_034033_20220419) in the binary snow maps (a-1, b-1, c-1). Overall, for higher FSC thresholds (FSC > 0.1 and 0.3), the binary snow maps showed slightly better results, while for the highest FSC threshold (FSC > 0.5), the snow-free areas of ASO_Snow were slightly overestimated. Additionally, we present statistical results of eight snow cover mapping algorithms using FSC thresholds of 0, 0.1, 0.3, and 0.5, illustrated in Fig. 3. The validation results demonstrated that nearly all snow cover mapping algorithms perform the worst when using FSC > 0, as evidenced by their lowest OA, F1_score, Kappa, and TSS. Employing FSC > 0 would result in an overestimation of snow cover area (see a-1, b-1, and c-1 of Fig. 2). This experiment highlights that this FSC threshold (FSC > 0) is not an optimal choice for determining snow-covered and snow-free at 30-pixelwise scale. Using seven metrics for analysis tests, we can conclude the optimal performance of eight snow cover mapping algorithms occurs when using the FSC threshold of 0.3, as reflected in overall metrics such as OA, F1_score, Kappa, and TSS (seeing Fig. 3). This finding differs significantly from previous study (Stillinger et al., 2023), which used FSC > 0 to distinguish snow-free and snow-covered areas at 120 m spatial resolution when using the 3 m ASO snow depth data.

To facilitate a comprehensive comparison of the eight snow cover mapping algorithms, Figs. 3 and 4 depict their performance against the 30-m ASO binary snow cover maps. This comparison considers four different FSC conversion thresholds and four land cover types. The analysis revealed that the performance of the algorithms vary significantly based on both the chosen FSC thresholds and the specific land cover types. Consequently, based on these findings, we categorized the eight algorithms into three groups. Group-1 algorithms, including Klein, Dozier, and SNOWMAP approaches, exhibited the best performance in mapping snow cover from Landsat surface reflectance data with the highest OA, F1_score, and Kappa. Multiple bands criteria were used to distinguish between snow-cover and snow-free, which was a common feature of these three algorithms. Differences in the performance of these three algorithms are apparent in forest type (Fig. 4). Based on the validation results, the Group-2 algorithm, namely NDSI_ONLY, NDSI_OTSU, Salomonson, and Sentinel_tanh, all based on NDSI, demonstrated comparable snow cover mapping capability across different land cover types and different FSC conversion thresholds, except for the case of FSC > 0 for Sentinel_tanh algorithm. At a 30 m pixel scale, fractional algorithms (Salomonson and Sentinel_tanh) had

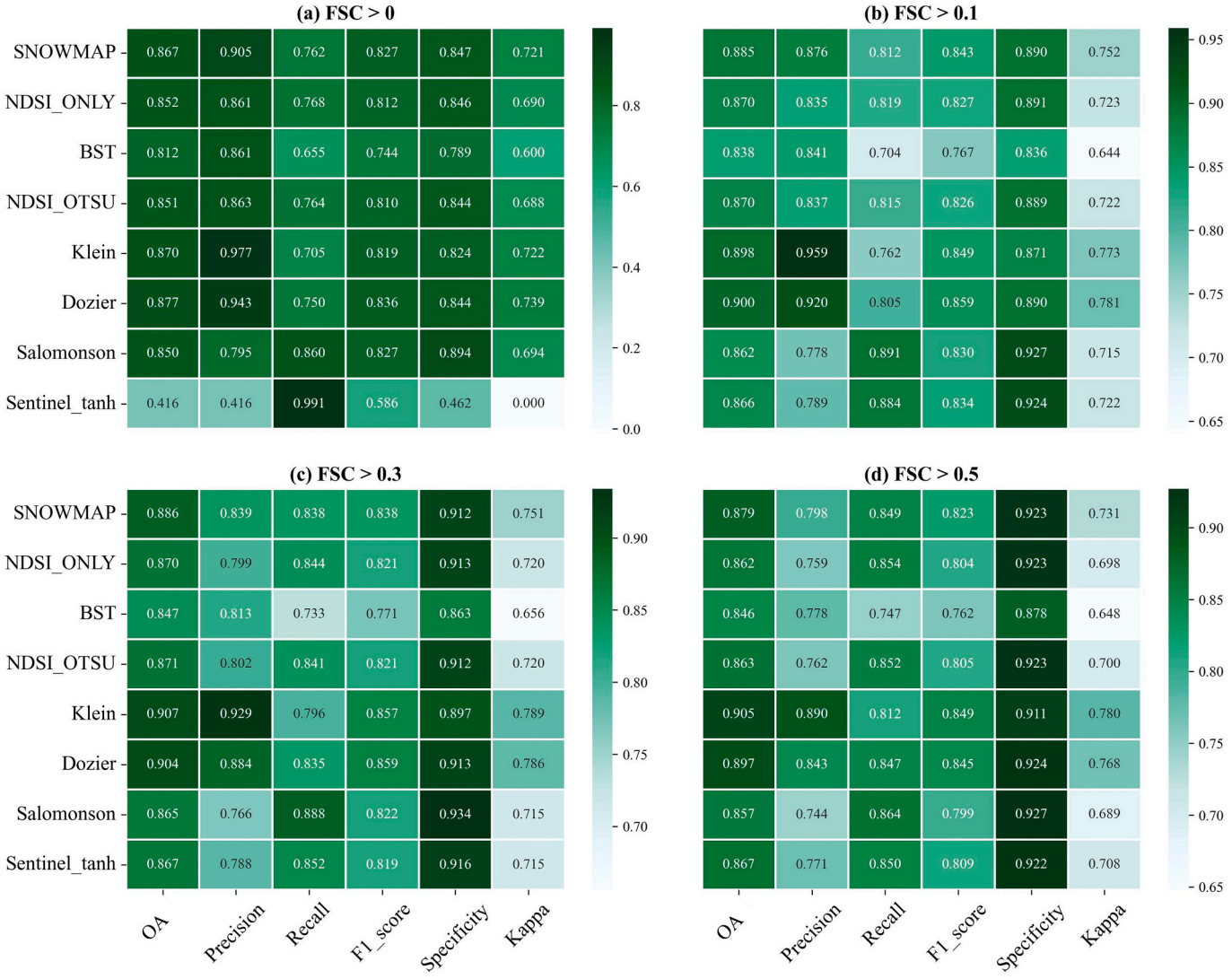

Fig. 3. Performance comparison of eight snow cover mapping algorithms under different thresholds of fractional snow cover conditions (FSC > 0, 0.1, 0.3, 0.5) against the reference ASO binary snow cover map (30 m).

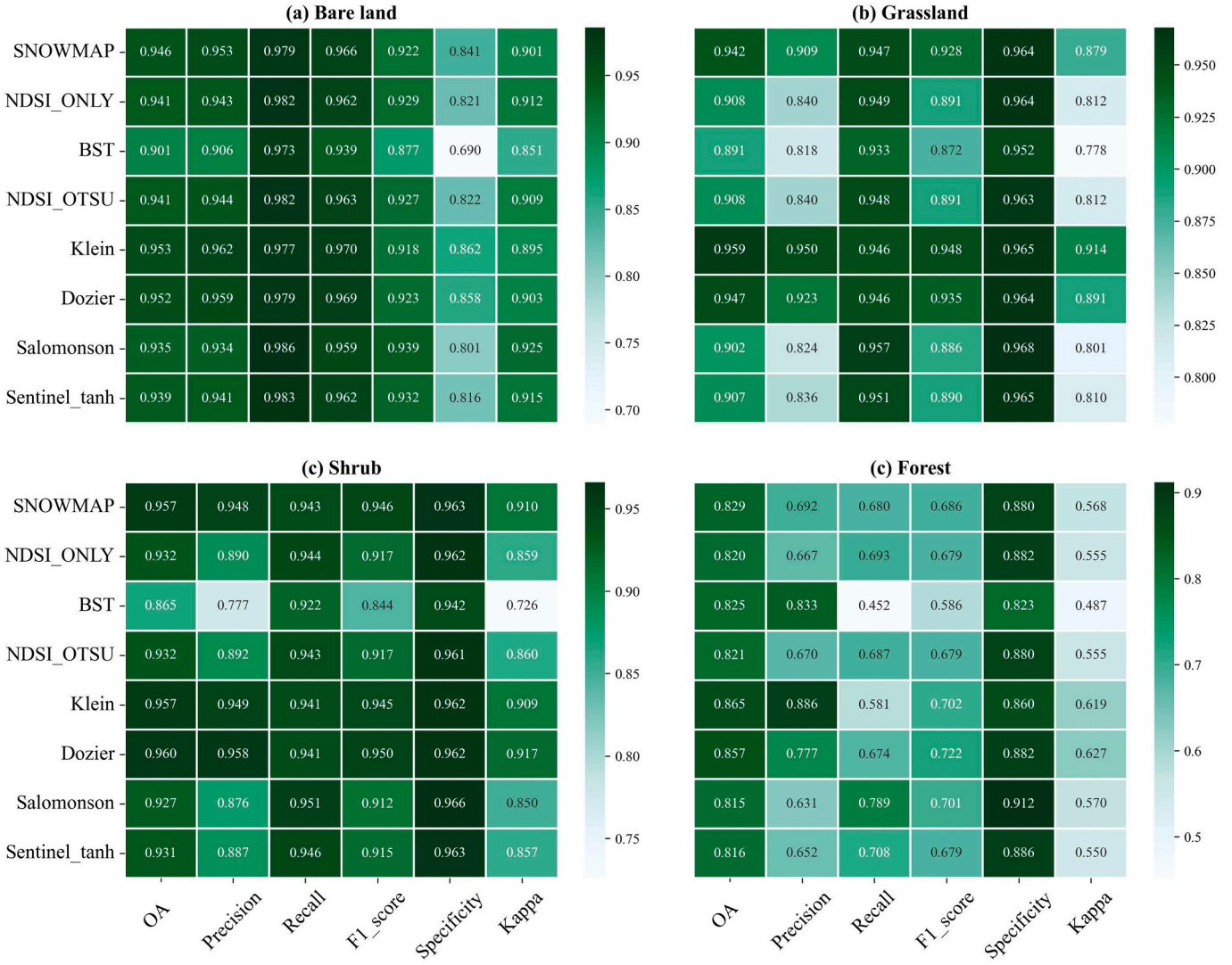

Fig. 4. Performance comparison of eight snow cover mapping algorithms using the FSC threshold of 0.3 under different land cover types, bare land (1,794,736), grassland (2,056,724), shrub (11,297,191), and forest (17,514,047) against the reference ASO binary snow cover map (30 m).

no obvious advantages in mapping snow cover over binary algorithms (NDSI_ONLY, NDSI_OTSU). BST algorithm belonged to Group-3, which used the blue band to identify snow-covered and snow-free areas and performed poorly compared to the other seven algorithms. The color of seven metrics of BST algorithms was close to white or light green, indicating that these metrics were the lowest in most cases, especially in forest areas (Fig. 4).

Land cover types play a significant role in mapping snow cover from satellite data, and its influence cannot be overlooked. Hence, we further characterized land cover effects on each snow cover mapping algorithm using an FSC conversion threshold of 0.3, as depicted in Fig. 4. The assessment reveals that the algorithms at the same capability group (Group-1, 2, 3) demonstrate comparable performance under the same land cover type. In addition, we observed that all snow cover algorithms showed better performance for bare land, grassland, and shrub land cover types. Nevertheless, forest areas remained a significant changes for most snow cover mapping algorithms compared to the other three land cover types (Xiao et al., 2022). This is evident, where forest-specific misclassification errors manifested as the highest commission error (1-Precision) and highest omission errors (1 - Recall). Notably, this trend occurred despite all eight snow cover mapping algorithms achieving OA greater than 0.8 within forest areas.

4.2. Impacts of snow cover mapping algorithms on snowline spatial determination

The spatial patterns of snowline depend on the binary snow map derived by each snow cover mapping algorithm. To visually illustrate the impacts of these algorithms on snowline delineation, a test region was chosen from the Landsat-8 (LC08_034033_20220419) image, as shown in the LD of Fig. 5. The confusion matrix maps from eight snow cover mapping algorithms against ASO 30 m binary snow map were displayed in Fig. 5, with true negative (TN; red) and true positive (TP; blue) representing the consistent classification of snow-free and snow-covered, respectively, and false negative (orange; FN) and false positive (green; FP) indicating disagreement in snow cover mapping for two snow cover maps. Additionally, there is an assumption that snow-free areas are located downhill from the snowline/mountain, while snow-covered areas are located uphill from the snowline/mountain.

Our findings revealed that the disagreement between 30-m ASO binary snow map and Landsat snow map derived by eight algorithms mainly occurred in forest areas, terrain shadow, and patchy snow areas close to the transition areas from snow-covered to snow-free. We also observed that Klein and BST algorithms had worse performance in mapping snow cover in terrain shadow, with a large proportion of these snow pixels classified as snow-free, resulting in a significant number of

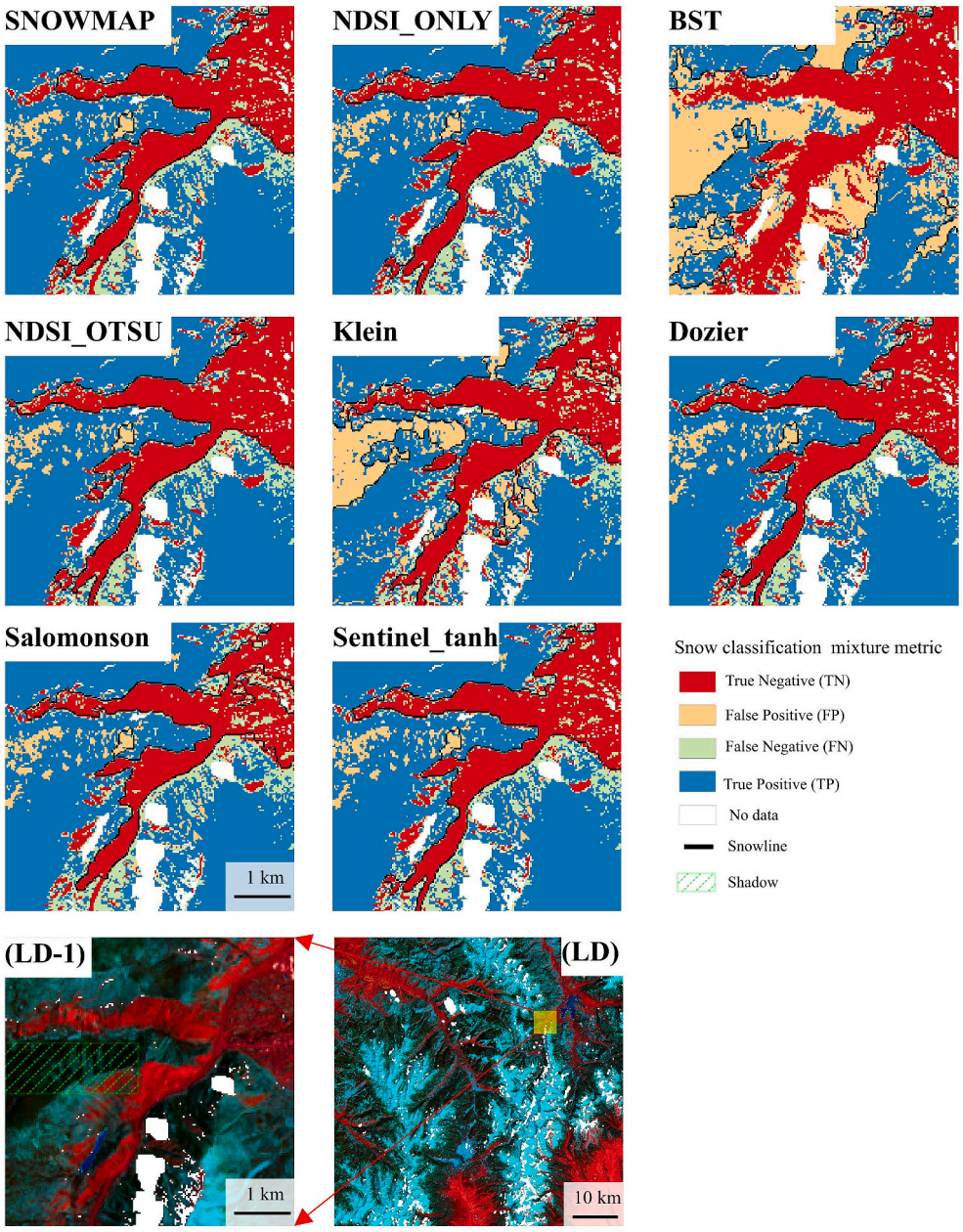

Fig. 5. Confusion matrix maps (true negative, false negative, false positive, and true positive) for the binary snow maps derived from eight snow cover mapping algorithms against the ASO binary snow cover map (30 m). LD: the false-color image (SWIR1/NIR/RED). The green hatching lines in the LD image (LC08_034033_20220419) at the Blue River site is an example of terrain shadow. Pixels denoted as no data are shown in white. Black lines in eight confusion matrix maps denote snowline we delineated. (For interpretation of the references to color in this figure legend, the reader is referred to the web version of this article.)

TN pixels. Moreover, the difference in snowline position was dependent on the ability of snow cover mapping algorithm. Eight snow cover mapping algorithms yielded considerably different shapes of snowline for the same area. The presence of large areas ($> 0.25\ km^2$) of FN and FP could extend the length of snowline, leading to inaccurate positioning regarding ASO snowline observations. The presence of FP would shift the snowline position downwards, while the presence of large areas of FN pixels would cause the actual snowline position to shift upwards.

We eliminated some misclassified pixels (FP and FN) by applying a series of snowline delineation steps (refer to Section 3.2) to minimize the uncertainty in snowline delineation resulting from snow cover misclassification. To investigate the impact of snow cover misclassification pixels (FP and FN) on the final snowline determination, we analyzed the proportion of these pixels using commission error (CE, $CE = FP/(TP + FP)$) and omission error (OE, $OE = FN/(TP + FN)$) relative to snowline position based on 25 ASO-Landsat image pairs, as exhibited in Fig. 6 and Table 3. For eight algorithms, our snowline delineation method successfully eliminated about 32% of CE (below snowline; average: 0.047, max: 0.082, min: 0.026) and 31% of OE (above snowline; average: 0.028, max: 0.044, min: 0.021), which ensure that these pixels did not impact snowline determination. However, approximately 68% of CE (above snowline; average: 0.101, max: 0.160, min: 0.064) and 69% of OE (below snowline; average: 0.063, max: 0.100, min: 0.036) were still present in binary snow map after the fourth step of snowline delineation method (removal of small snow-free areas), and they affected the determination of the shape and position of snowline. This, in turn, made the bottom 10% snowline elevation lower due to the increase of above snowline CE, while larger below snowline OE may partially explain the higher top 10% snowline elevation (further analysis showing in Section 4.4).

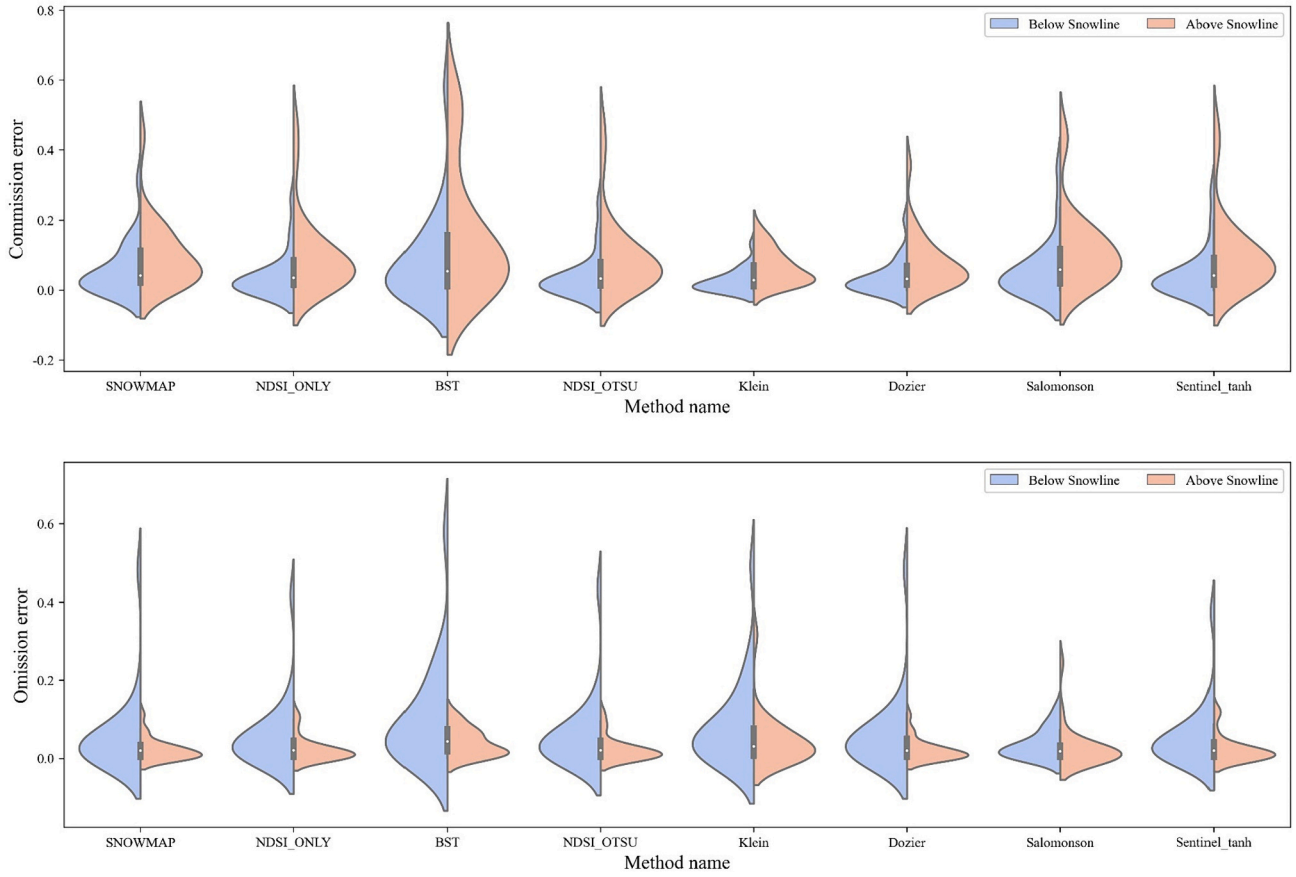

Fig. 6. Distribution of commission error ($CE = FP/(TP + FP)$) and omission error ($OE = FN/(TP + FN)$) relative to snowline (below and above snowline) for 25 snow cover maps obtained from eight snow cover mapping algorithms.

Table 3
Average values of commission error and omission error under below and above snowline conditions, respectively, for snow cover maps obtained from eight snow cover mapping algorithms. Commission error: $CE = FP/(TP + FP)$; Omission error: $OE = FN/(TP + FN)$. Bold indicates the maximum of each column.

Name	Commission Error		Omission Error	
	Below snowline	Above snowline	Below snowline	Above snowline
SNOWMAP	0.056	0.097	0.054	0.022
NDSI_ONLY	0.040	0.097	0.057	0.022
BST	**0.082**	**0.160**	**0.100**	0.040
NDSI_OTSU	0.038	0.096	0.058	0.022
Klein	0.026	0.064	0.083	**0.044**
Dozier	0.034	0.077	0.060	0.021
Salomonson	0.057	0.117	0.036	0.027
Sentinel_tanh	0.045	0.102	0.052	0.022
Average values	0.047	0.101	0.063	0.028

4.3. Analysis spatial pattern of snowline delineation results

In this study, Landsat binary snow maps obtained through snow cover mapping algorithms were used to automatically delineate snowline using a series of data processing steps (refer to Section 3.2; Fig. 1). The spatial pattern of snowline represents the extent of snow cover, and ideally should capture the boundary of binary snow map. Our proposed snowline delineation method created a robust snowline pattern for each binary snow map (Fig. 7). This method avoided the creation of fragmented snowline patterns in the vicinity of small snow-free and snow-covered areas of binary snow map. It was more consistent with the patterns and locations of snowlines that we visually inspected from binary snow map. Our developed snowline delineation method demonstrates the capability to effectively eliminate misclassified pixels and accurately determine a continuous snowline. Furthermore, this new approach to snowline delineation can overcome the effects of no data in a limited area (Girona-Mata et al., 2019), where pixels without data may lead to incorrect snowline patterns or fail to provide a continuous snowline.

The Landsat false-color image (Fig. 8) presents the snow cover distribution case along with snowline, and the binary snow cover map for eight algorithms is referred to in Fig. 7. Commission errors and omission errors in binary snow maps can change snowline patterns for the same area due to differences in the use of snow cover mapping algorithms (Figs. 7 and 8). Visual inspection in Fig. 8 helped us better understand the performance of binary snow cover associated with snowline. As discussed in Section 4.1, shadow areas seriously affected the accuracy of binary snow cover map and snowline pattern for BST and Klein algorithms. Even for the reference ASO snow observation, there were still misclassified pixels (yellow dashed box areas), as shown in Figs. 7 and 8, and this data's limitations were further discussed in Section 5.1. Therefore, we concluded that achieving a high level of accuracy in snowline depends on the quality of binary snow maps.

4.4. Difference assessment on snowline elevation

Figure 9 presents an example to highlight the variation in snowline elevation determined by different snow cover mapping algorithms. It showcases the ASO binary snow map for the ASO-USCATE-20160401 scene in the Tuolumne Cherry/Eleanor basin, California, along with the corresponding snowline elevation distributions derived from ASO_Snow and eight snow cover mapping algorithms. The results reveal

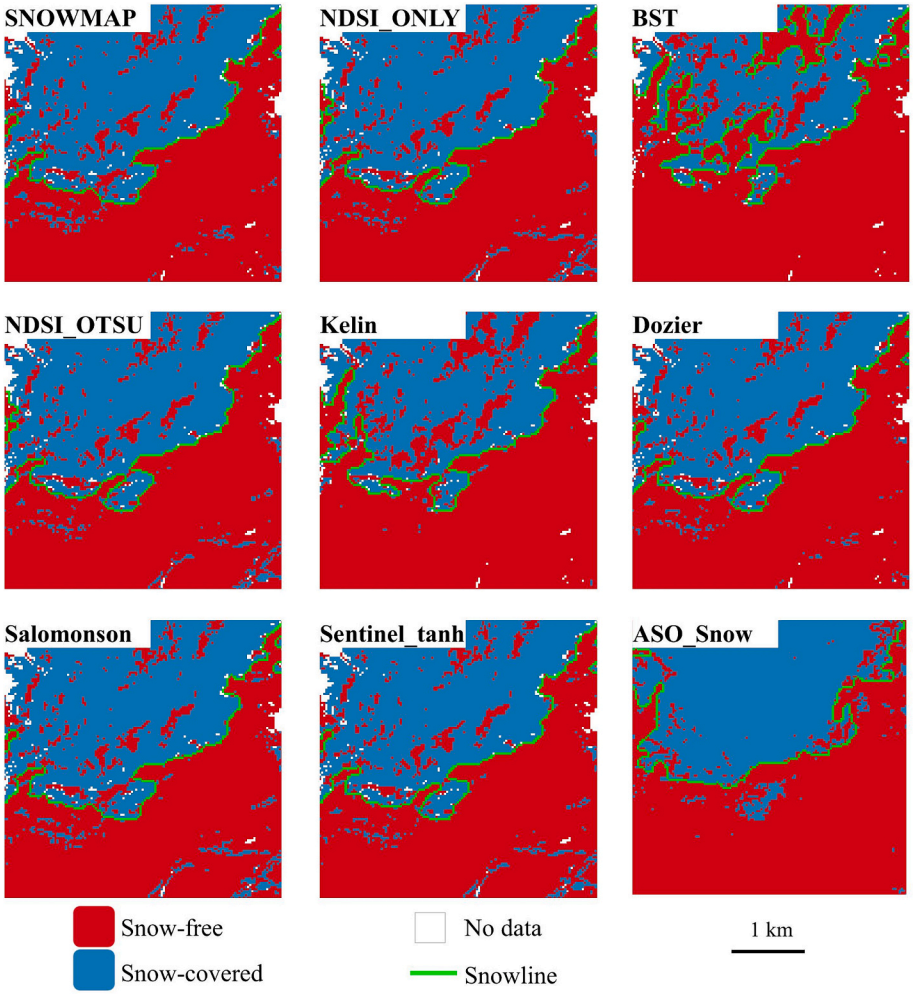

Fig. 7. Distribution of snowlines for nine snow cover algorithms at a small region of the Tuolumne Cherry/Eleanor basin, California (USCATE) in Landsat image (LC08_043033_20,160,401). The background shows the binary snow cover. The green line refers to the snowline. ASO_Snow denotes the reference ASO snow cover data. (For interpretation of the references to color in this figure legend, the reader is referred to the web version of this article.)

significant differences in both the pattern and distribution of snowline elevation across the different algorithms for the same study basin. Notably, the average snowline elevation varied considerably, ranging from 1907 m (lowest) for the SNOWMAP algorithm to 2184 m (highest) for the BST algorithm. While the snowline elevation density analysis image exhibits the similar distribution patterns across all nine algorithms, it also highlights distinct differences in the peaks and the ranges of their respective snowline elevation densities.

Beyond the specific case presented in Fig. 9, we conducted a comprehensive comparative analysis of snowline elevations across 25 ASO-Landsat images pairs. This analysis, as illustrated in Figs. 10 and 11, utilized three metrics: bottom 10% snowline elevation, average snowline elevation, and top 10% snowline elevation. These metrics served to assess the spatial agreement of snowline elevations between different methods. The results, presented in the subplots of Figs. 10 and 11, consistently revealed a negative elevation difference across most study basins. In simpler terms, the snowline elevations derived from Landsat data were lower than those obtained from ASO observations (ASO_Snow) snowlines. This finding aligns with the observations from Figs. 7 and 8, where ASO_Snow snowline results were consistently at higher elevations relative to Landsat-based snowlines.

The disparities in snowline elevations derived from different snow cover mapping algorithms are substantial for all conditions. For instance, among the eight algorithms examined, the difference of average snowline elevation ranged from 121 m to 258 m. Differences in the bottom 10% snowline elevations fell within the range of 253 m to 512 m, while for the top 10%, the differences spanned from 206 m to 344 m. As illustrated in Fig. 10 and Table 4, the Klein and Dozier algorithms displayed relatively smaller snowline elevation differences compared to ASO snowline elevation across all three metrics. This consistency is likely due to their high snow mapping accuracy (Figs. 3 and 4), particularly their notably low above snowline CE (Klein: 0.064, Dozier: 0.077; Table 3 and Fig. 6). In contrast, the BST algorithm, which had the largest above snowline CE (0.16), demonstrated the largest elevation difference, especially in the bottom 10% snowline elevation (-332 ± 663 m). Additionally, as illustrated in Fig. 11 and Table 5, the Klein and Dozier algorithms consistently displayed the lower snowline elevation differences across all aspect conditions (North, South, East, and West). Moreover, when comparing to the four aspects, east and south aspects exhibited lower difference values in snowline elevation across all three snowline elevation metrics. Notably, as shown in Fig. 10 and Table 4, the ranking of elevation differences in the bottom 10% snowline elevation almost correlates with the ranking of above snowline CE. This correlation suggests that higher above snowline CE may lead to lower snowline elevations relative to the ASO reference data, a trend visibly evident in Figs. 7 and 8. Meanwhile, below snowline OE partially explain the differences observed in the top 10% snowline elevation. Misclassifying snow pixels as snow-free below the snowline can

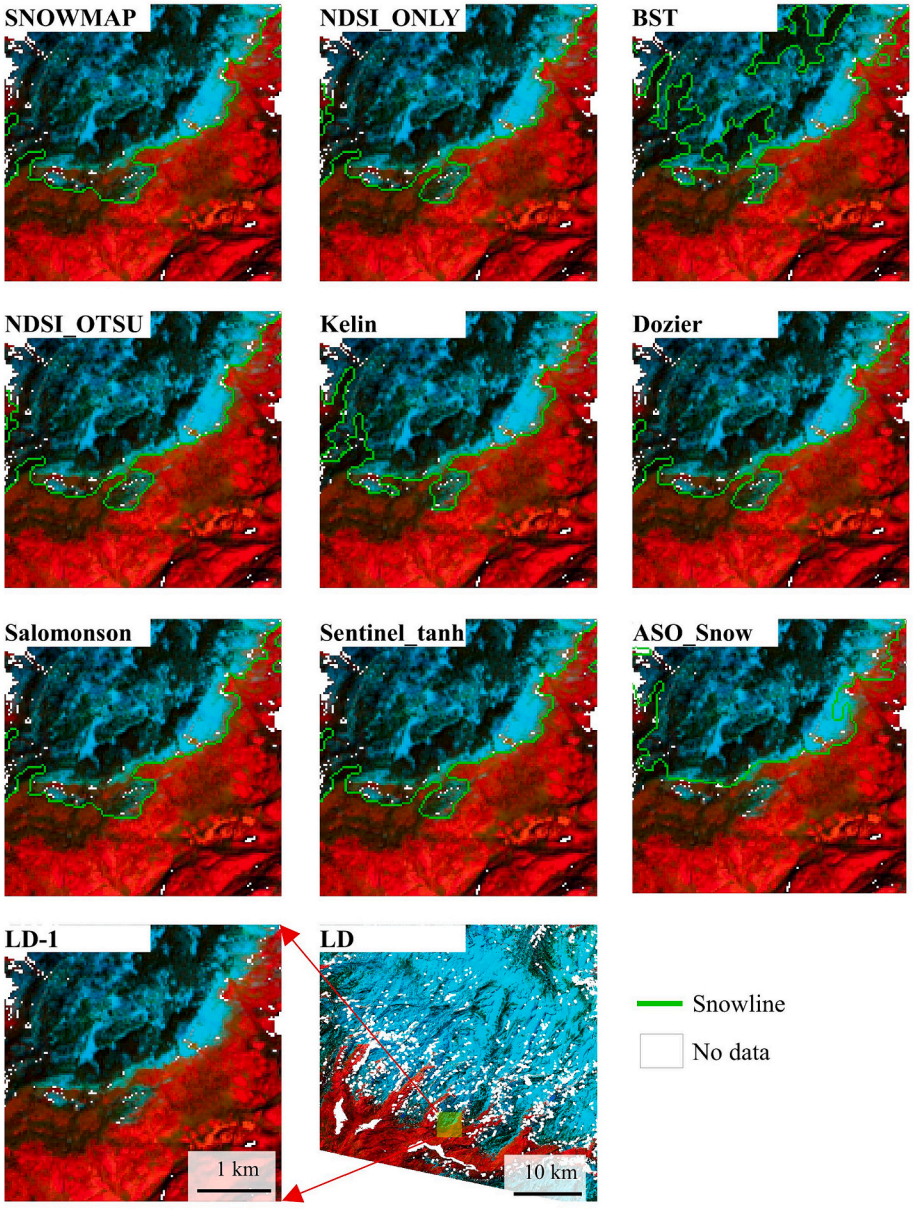

Fig. 8. Distribution of snowlines for nine snow cover algorithms at a small region of the Tuolumne Cherry/Eleanor basin, California (USCATE) in Landsat image (LC08_043033_20,160,401). The background shows the Landsat false-color image (SWIR1/NIR/RED). The green line refers to the snowline. ASO_Snow denotes the reference ASO snow cover data. (For interpretation of the references to color in this figure legend, the reader is referred to the web version of this article.)

potentially shift the perceived snow boundary upwards. These findings suggest that CE exerts a greater influence on snowline determination than OE.

5. Discussion

5.1. Uncertainty in using ASO snow-depth data

ASO snow depth data is widely recognized as the highest quality snow observation data for various snow-related research. However, it is unrealistic to assume that ASO data is a perfectly accurate snow measurement treated as a validation or reference for "true" ground observations by other researchers. Before using ASO 3 m snow depth data for further processing, it is essential to address the misrepresentation issues first (Stillinger et al., 2023). Failure to do so can result in inaccurate validation and false snowline maps. As illustrated in Fig. S1 in the Supplement, there should be no data in the yellow arrows area, but the zero values were assigned. Then snowline was portrayed based on our snowline delineation method. No snowline should exist at the boundary of these misrepresentation areas.

The binary snow maps derived from ASO snow depth products are not immaculate in validating Landsat snow maps due to false snow-free and snow-covered pixels. The accuracy of LiDAR data is often poor in steep terrain and densely forested areas, resulting in varying quality of snow depths obtained from LiDAR data (Currier et al., 2019; Enderlin et al., 2022; Zheng et al., 2016). Moreover, ASO may consider rock outcrops areas in alpine regions to be completely covered with snow, as discussed in a previous study (Stillinger et al., 2023). The false pixels in ASO binary snow maps would lead to unreal evaluation results, seeing the results in Sections 4.1 and 4.3.

It is necessary to analyze the conversion of FSC to binary snow when evaluating snow cover at 30 m pixel-wise (John et al., 2022; Stillinger et al., 2023). This study conducted sensitive tests to select an optimal threshold for converting ASO FSC data to binary snow maps. However,

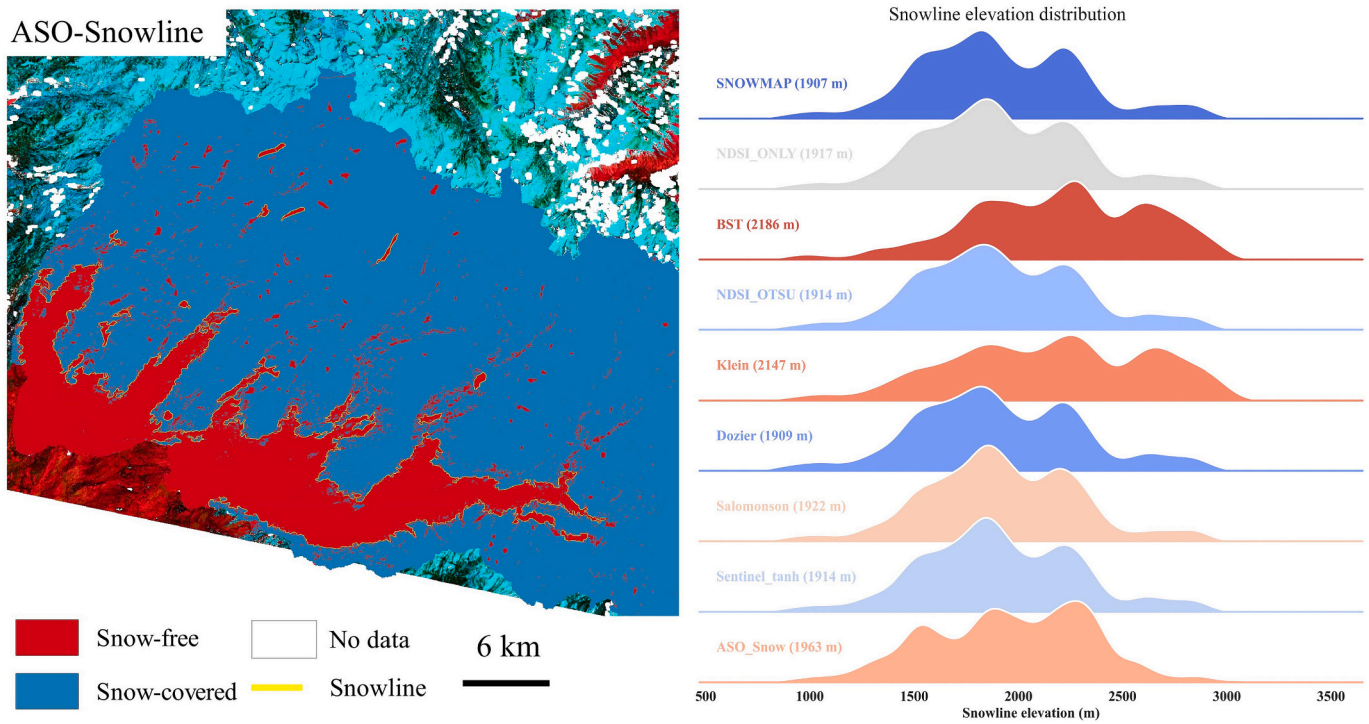

Fig. 9. Left panel illustrates the reference ASO binary snow map (30 m; red pixels are snow-free and blue pixels are snow-covered) and the distribution of snowline (green line) in the ASO-USCATE-20160401 scene (Tuolumne Cherry/Eleanor basin, California); the background is Landsat false-color image (SWIR1/NIR/RED). The right panel shows the distribution of snowline elevation in the left study area (Tuolumne Cherry basin, California) for nine snow cover mapping algorithms. ASO_Snow is the reference ASO snow cover data. The number in parentheses indicate the average snowline elevation in the Tuolumne Cherry/Eleanor basin. (For interpretation of the references to color in this figure legend, the reader is referred to the web version of this article.)

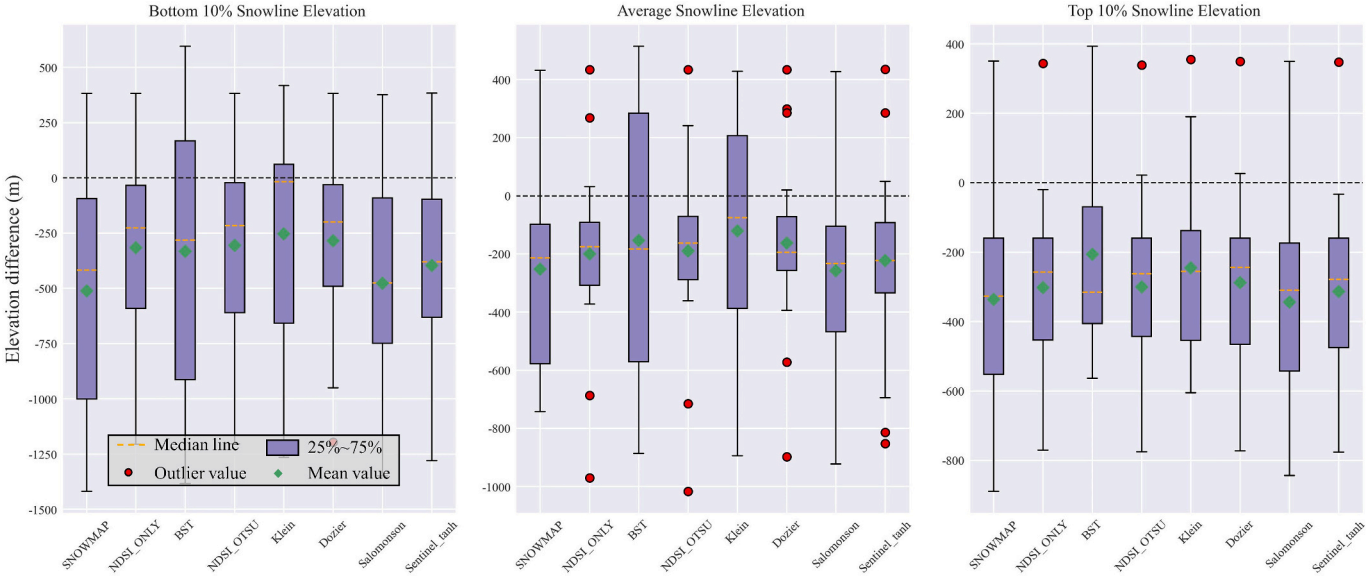

Fig. 10. Snowline elevation difference in bottom 10% snowline elevations, average snowline elevation, and top 10% snowline elevations for 25 Landsat snowline elevation data derived from eight snow cover mapping algorithms with respect to the reference ASO snowline elevation.

we still encountered false negative snow-free observations within ASO binary snow maps due to thin snow and patch snow (Figs. 2, 7, and 8), using the FSC threshold of 0.3. Some shallow or patch snow pixels may be lost when converting snow depths to binary snow data using a threshold of 8 cm (Painter et al., 2016), leading to false negatives. Moreover, compared to Lidar-based reference snow observation, most snow cover mapping approaches estimated more snow cover pixels (CE > OE). We found that misclassification pixels of ASO binary snow map (30 m) mainly occurred near the edge of snow cover extent. Loss of snow-covered pixels not only increases the inconsistency between reference ASO binary snow map and Landsat binary snow map for eight algorithms, decreasing the evaluation metrics but also raises the elevation of ASO snowline, as illustrated in Fig. 10. This inconsistency was amplified in analyzing snowline elevation difference between ASO data and Landsat data in Section 4.4 (Fig. 10 vs. Fig. 11). Despite limitations in ASO data for snow-related research, particularly snowline studies, our

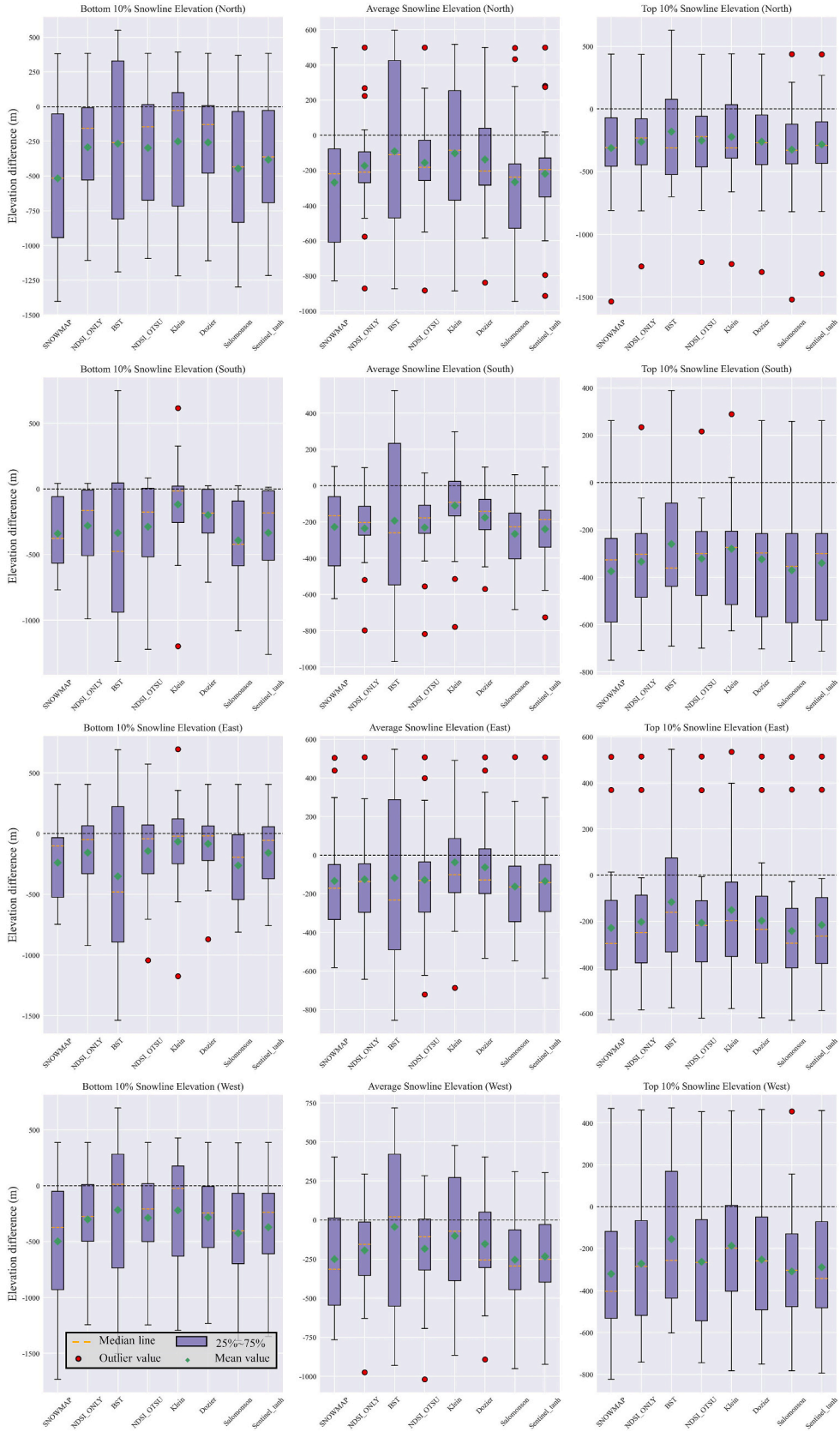

Fig. 11. Snowline elevation difference in bottom 10% snowline elevation, average snowline elevation, and top 10% snowline elevation for 25 Landsat snowline elevation data derived from eight snow cover mapping algorithms with respect to the reference ASO snowline elevation for different aspects.

Table 4
Statistics analysis of snowline elevation difference in bottom 10% snowline elevation, average snowline elevation, and top 10% snowline elevation for 25 Landsat snowline elevation data derived from eight snow cover mapping algorithms with respect to the reference ASO snowline elevation (cf. Fig. 10). The number in the table denotes mean elevation difference ± 1 standard deviation.

Algorithm name	Bottom 10% snowline elevations /m	Average snowline elevation /m	Top 10% snowline elevations /m
SNOWMAP	−512 (±527)	−252 (±335)	−336(±282)
NDSI_ONLY	−315 (±382)	−199 (±285)	−302 (±268)
BST	−332 (±663)	−154 (±479)	−206 (±295)
NDSI_OTSU	−306 (±391)	−190 (±292)	−300 (±272)
Klein	−253 (±541)	−121 (±385)	−245 (±269)
Dozier	−285 (±381)	−163 (±285)	−288 (±270)
Salomonson	−478 (±464)	−258 (±313)	−344 (±271)
Sentinel_tanh	−396 (±436)	−223 (±303)	−313 (±269)

Table 5
Statistics analysis of snowline elevation difference in bottom 10% snowline elevation, average snowline elevation, and top 10% snowline elevation for 25 Landsat snowline elevation data derived from eight snow cover mapping algorithms with respect to the reference ASO snowline elevation for different aspects (cf. Fig. 11). The number in the table denotes mean elevation difference ± 1 standard deviation.

Aspect	Algorithm name	Bottom 10% snowline elevation /m	Average snowline elevation /m	Top 10% snowline elevation /m
North	SNOWMAP	−517 (±532)	−269 (±401)	−312 (±432)
	NDSI_ONLY	−294 (±399)	−175 (±296)	−263 (±394)
	BST	−267 (±625)	−91 (±527)	−180 (±411)
	NDSI_OTSU	−297 (±412)	−157 (±289)	−253 (±395)
	Klein	−251 (±532)	−104 (±444)	−223 (±392)
	Dozier	−258 (±403)	−139 (±324)	−260 (±405)
	Salomonson	−446 (±484)	−266 (±368)	−325 (±423)
	Sentinel_tanh	−383 (±447)	−220 (±339)	−283 (±401)
South	SNOWMAP	−339 (±299)	−228 (±222)	−374 (±255)
	NDSI_ONLY	−280 (±335)	−235 (±204)	−334 (±236)
	BST	−335 (±659)	−194 (±478)	−259 (±310)
	NDSI_OTSU	−288 (±372)	−231 (±211)	−322 (±234)
	Klein	−118 (±400)	−110 (±276)	−280 (±248)
	Dozier	−199 (±222)	−176 (±175)	−324 (±244)
	Salomonson	−391 (±335)	−267 (±195)	−371 (±256)
	Sentinel_tanh	−333 (±376)	−240 (±204)	−340 (±248)
East	SNOWMAP	−240 (±318)	−134 (±294)	−229 (±299)
	NDSI_ONLY	−157 (±350)	−126 (±289)	−203 (±283)
	BST	−352 (±668)	−118 (±479)	−116 (±322)
	NDSI_OTSU	−144 (±393)	−128 (±317)	−206 (±282)
	Klein	−66 (±394)	−37 (±307)	−151 (±284)
	Dozier	−84 (±290)	−63 (±279)	−198 (±294)
	Salomonson	−263 (±346)	−163 (±279)	−242 (±290)
	Sentinel_tanh	−158 (±333)	−134 (±290)	−216 (±284)
West	SNOWMAP	−499 (±601)	−249 (±372)	−320 (±339)
	NDSI_ONLY	−302 (±420)	−195 (±309)	−270 (±322)
	BST	−214 (±674)	−44 (±526)	−155 (±339)
	NDSI_OTSU	−287 (±427)	−185 (±316)	−262 (±327)
	Klein	−221 (±567)	−102 (±416)	−187 (±318)
	Dozier	−283 (±436)	−153 (±327)	−252 (±326)
	Salomonson	−426 (±515)	−254 (±340)	−308 (±323)
	Sentinel_tanh	−372 (±491)	−233 (±345)	−288 (±332)

work highlights the importance of uncertainty mitigation and robust benchmarking in enhancing the accuracy of snow cover mapping and snowline delineation.

5.2. Insights of snow cover mapping algorithms comparison

AVHRR and MODIS data are commonly used to estimate snow cover area in numerous pieces of research, with Landsat snow observation often serving as the benchmarks for validation or calibration (Rittger et al., 2013; Wu et al., 2020; Xiao et al., 2022). With reference to ASO 3 m snow observations, in this study, we examined the snow mapping capability of eight snow cover mapping algorithms using Landsat surface reflectance data. Our findings indicate that no single algorithm outperformed all others in all conditions.

The comparable performance of the SNOWMAP (Hall et al., 1995) and Dozier (Dozier and Painter, 2004) approaches in snow cover mapping can be attributes largely to the high similarity in their decision tree rules. The primary distinction between these algorithms lies in their snow detection rules in vegetation area. As Fig. 4 clearly demonstrates, the most significant difference in their performance arises in mapping snow cover and estimating snow cover area with forest areas, while their performance exhibits greater consistency across other land cover types. Dynamic thresholds for NDSI typically performed better than static thresholds in snow cover area estimations, as the optimal threshold varies with Landsat image (Yin et al., 2013). Still, these significant advantages did not manifest in our evaluation results of NDSI_OTSU versus NDSI_ONLY. Instead, their mapping capabilities are very similar in identifying snow cover (Section 4.1). This similarity may be mainly due to the average optimal NDSI threshold of 0.4842 obtained from NDSI_OTSU algorithm (Table S2 in the Supplement), which closely approximates the threshold of 0.45 used in NDSI_ONLY algorithm. The balanced number of snow-covered and snow-free pixels is crucial for conducting NDSI_OTSU algorithm (Härer et al., 2018; Yin et al., 2013), and the disordered bias in the number of pixels toward any class can result in large errors in the snow cover classification results. The BST algorithm was originally developed for high-resolution remote sensing imagery (3–5 m) to map snow cover area, as described in Thaler et al. (2023). This study represents the BST algorithm has been applied to Landsat images with a coarser resolution of 30 m. Our results revealed a significant concentration of misclassification errors occurring within shadowed and forested areas (Figs. 5, 7 and 8), resulting underestimating snow cover areas. Coarser resolution, shading, and tree occlusion collectively result in lower reflectance of snow in the blue band for shadowed and forested areas compared to open, flat areas (Thaler et al., 2023). And then this lower reflectance can mislead the BST algorithm and lead to misclassification of snow pixels.

As mentioned, forest cover is the major factor impacting snow cover mapping performance for all algorithms and contributing to serious classification errors. Previous studies have developed different canopy adjustments/correction approaches to alleviate uncertainties in estimating snow cover area using Landsat and MODIS surface reflectance data in forested areas (Bair et al., 2020; Raleigh et al., 2013; Rittger et al., 2020; Xiao et al., 2022). In a recent evaluation experiment (Stillinger et al., 2023), they coupled different canopy correction methods with each snow cover fraction estimation algorithm to analyze the algorithm's performance in estimating viewable snow cover areas in various vegetation coverages. However, the viewable snow cover area observed by satellite sensors varies with view zenith angle, solar zenith angle, and canopy cover fractions (Rittger et al., 2020; Xiao et al., 2022). Previous studies (Kostadinov et al., 2019; Xiao et al., 2022) have reported that canopy correction process can also introduce uncertainties in fractional snow cover estimation. It remains a significant challenge to estimate viewable snow cover areas from satellite data (e.g., Lidar, Landsat, and MODIS) in forest cover regions.

5.3. Insights of snowline delineation method

This study introduces a novel, automated snowline delineation method (i.e., ASLD-BSC), designed to accurately extract the snow boundary from binary snow maps. We evaluated the proposed ASLD-BSC method by applying various snow cover mapping algorithms to Landsat imagery and using the resulting binary snow maps as input for ASLD-BSC method, leveraging principles of vision inspection. We further explored the applicability of ASLD-BSC method to MODIS snow cover maps for delineating a MODIS-based snowline (Fig. S2 in the Supplement). The results demonstrate that ALSD-BSC method

effectively delineates the snowline from MODIS binary snow maps generated by two different algorithms. The analysis confirmed the excellent capability of ASLD-BSC method to accurately extract snowlines. Additionally, a comparison between Landsat snowlines (Fig. 7) and MODIS snowlines (Fig. S2) for the same study area (Tuolumne Cherry/Eleanor basin, California) highlights the limitations associated with the coarser resolution of MODIS data. This coarseness leads to a significant presence of mixed pixels within the six gullies in the MODIS maps (Fig. S2 in the Supplement), hindering the distinction between snow-free and snow-covered pixels. Consequently, the MODIS snow boundary (or snowline) differs significantly from the detailed snow distribution and boundary depicted by the eight individual snow cover maps derived from Landsat data in this mountainous area (Fig. 7). Additionally, compared to eight binary snow cover maps derived from Landsat, both MODIS-based maps obviously overestimated the snow cover area in this testing area.

Our analysis revealed remarkable discrepancies in snowline elevation across different aspects (north, south, east, and west) among the eight algorithms tested. This finding contradicts previous studies (Gascoin et al., 2019; Krajčí et al., 2014; Portenier et al., 2022) that assumed a uniform snowline elevation for all aspects. To further investigate these variations, we compared the proposed ASLD-BSC method with a widely used approach, the RSL method (Krajčí et al., 2014), in two testing areas (see Figs. S3 and S4 in the Supplement). It's important to note that the RSL method is only applicable to the basin area (Girona-Mata et al., 2019; Krajčí et al., 2014) and requires preprocessing of the input image into smaller basin before employing, limiting its use in larger or more complex study areas. As shown in Figs. S3 and S4, the proposed ASLD-BSC effectively captured the snow boundary between snow-free and snow-covered areas, while the RSL method's snowlines did not accurately represent the actual snow cover extent (Koehler et al., 2022). Notably, the RSL method produced the same snowline elevation across all aspects for nine testing algorithms. This discrepancy likely stems from the RSL method's inability to account for the complex impact of topography on snow cover distribution, area, and location, as influenced by factors like slope gradient, aspect, and elevation (Grünewald et al., 2014; Zhong et al., 2021). The complexity distribution of snow cover naturally leads to variations in snowline patterns and elevations across different aspects, as evident in the results generated by the ASLD-BSC method. These observed variations in snowline elevation likely stem from differential impacts of factors such as solar radiation and surface land cover, as previously discussed in Girona-Mata et al. (2019). However, the RSL results also highlighted the significant influence of snow cover mapping algorithm accuracy on snowline delineation, demonstrating a maximum difference of 99 m in elevation among the nine RSL snowlines.

6. Conclusions

This study comprehensively evaluated and compared the efficacy of eight snow cover mapping algorithms in accurately delineating binary snow cover from Landsat images and determining snowline in mountainous areas. In addition, a novel snowline delineation method, consisting of a series of automated processing chains, was proposed, and we quantified the uncertainties of snow cover mapping algorithm in defining snowline using 25 Landsat-ASO image pairs.

The comparison findings revealed that eight snow cover mapping algorithms can be categorized into three groups. Group-1 algorithms (Klein, Dozier, and SNOWMAP), incorporating additional snow-related variables and decision rules, demonstrated the most robust performance. Group-2 algorithms, encompassing NDSI_ONLY, NDSI_OTSU, Salomonson, and Sentinel_tanh, showed moderate performance, while Group-3 category (BST) displayed the least favorable performance. The investigation into the influence of eight snow cover mapping algorithms on determining snowline revealed that the proposed snowline delineation method, ASLD-BSC, effectively eliminated a substantial portion of misclassification pixels (32% of CE and 31% of OE), but a significant proportion (68% of CE and 69% of OE) still impacted the delineation of the snowline's pattern. Moreover, the evaluation of snowline elevation unveiled substantial elevation differences among eight snow cover mapping algorithms relative to the reference ASO snowline elevations (average snowline elevation: 121 m ~ 258 m; bottom 10% snowline elevation: 253 m ~ 512 m; top 10% snowline elevation: 206 m ~ 344 m), even when they exhibited similar performance in snow cover mapping. Our analysis highlights the significant influence of snow cover mapping algorithm accuracy on snowline delineation derived from Landsat imagery.

This study significantly advances our understanding of the ability of snow cover mapping algorithm and snowline delineation using Landsat images. Importantly, it emphasizes the significance of accounting for systematic biases inherent to different snow cover mapping algorithms when interpreting snowline delineation and variation. The promising results of ASLD-BSC suggest its potential for flexible adaption and application across diverse mountainous regions. This capability of defining the snowline with greater precision holds significant values for risk assessments in new snow-free areas and ecological impact assessments of rising snow levels (Bosson et al., 2023). Future research will validate the effectiveness across more diverse geographical landscapes and providing accurate snow cover and snowline pattern maps.

CRediT authorship contribution statement

Xiongxin Xiao: Conceptualization, Investigation, Methodology, Visualization, Writing – original draft. **Shuang Liang:** Conceptualization, Investigation, Writing – review & editing.

Declaration of competing interest

The authors declare that they have no known competing financial interests or personal relationships that could have appeared to influence the work reported in this paper.

Data availability

The authors do not have permission to share data.

Acknowledgment

The authors gratefully acknowledge the support for this research from the National Natural Science Foundation of China (No. 42201148). We appreciate help from Evan A. Thaler (Earth and Environment Sciences Division, Los Alamos national laboratory, USA), Edward H. Bair (Earth Research Institute, University of California, Santa Barbara, USA), Yichuan Ma (School of Remote Sensing and Information Engineering, Wuhan University, China), and Xiaoyi Wang (Institute of Tibetan Plateau Research, Chinese Academy of Sciences, China).

Appendix A. Supplementary data

Supplementary data to this article can be found online at https://doi.org/10.1016/j.rse.2024.114163.

References

Bair, E.H., Stillinger, T., Dozier, J., 2020. Snow property inversion from remote sensing (SPIReS): a generalized multispectral Unmixing approach with examples from MODIS and Landsat 8 OLI. IEEE Trans. Geosci. Remote Sens. 59, 7270–7284. https://doi.org/10.1109/TGRS.2020.3040328.

Barnett, T.P., Adam, J.C., Lettenmaier, D.P., 2005. Potential impacts of a warming climate on water availability in snow-dominated regions. Nature 438, 303–309. https://doi.org/10.1038/nature04141.

Berghuijs, W.R., Woods, R.A., Hrachowitz, M., 2014. A precipitation shift from snow towards rain leads to a decrease in streamflow. Nat. Clim. Chang. 4, 583–586. https://doi.org/10.1038/nclimate2246.

Bishop-Taylor, R., Nanson, R., Sagar, S., Lymburner, L., 2021. Mapping Australia's dynamic coastline at mean sea level using three decades of Landsat imagery. Remote Sens. Environ. 267, 112734 https://doi.org/10.1016/j.rse.2021.112734.

Bosson, J.B., Huss, M., Cauvy-Fraunié, S., Clément, J.C., Costes, G., Fischer, M., Poulenard, J., Arthaud, F., 2023. Future emergence of new ecosystems caused by glacial retreat. Nature 620, 562–569. https://doi.org/10.1038/s41586-023-06302-2.

Brandt, W.T., Bormann, K.J., Cannon, F., Deems, J.S., Painter, T.H., Steinhoff, D.F., Dozier, J., 2020. Quantifying the spatial variability of a snowstorm using differential airborne Lidar. Water Resour. Res. 56, 1–22. https://doi.org/10.1029/2019WR025331.

Currier, W.R., Pflug, J., Mazzotti, G., Jonas, T., Deems, J.S., Bormann, K.J., Painter, T.H., Hiemstra, C.A., Gelvin, A., Uhlmann, Z., Spaete, L., Glenn, N.F., Lundquist, J.D., 2019. Comparing aerial Lidar observations with terrestrial Lidar and snow-probe transects from NASA's 2017 SnowEx campaign. Water Resour. Res. 55, 6285–6294. https://doi.org/10.1029/2018WR024533.

Czyzowska-Wisniewski, E.H., van Leeuwen, W.J.D., Hirschboeck, K.K., Marsh, S.E., Wisniewski, W.T., 2015. Fractional snow cover estimation in complex alpine-forested environments using an artificial neural network. Remote Sens. Environ. 156, 403–417. https://doi.org/10.1016/j.rse.2014.09.026.

Dobreva, I.D., Klein, A.G., 2011. Fractional snow cover mapping through artificial neural network analysis of MODIS surface reflectance. Remote Sens. Environ. 115, 3355–3366. https://doi.org/10.1016/j.rse.2011.07.018.

Dozier, J., Painter, T.H., 2004. Multispectral and hyperspectral remote sensing of alpine snow properties. Annu. Rev. Earth Planet. Sci. 32, 465–494. https://doi.org/10.1146/annurev.earth.32.101802.120404.

Dozier, J., Bair, E.H., Baskaran, L., Brodrick, P.G., Carmon, N., Kokaly, R.F., Miller, C.E., Miner, K.R., Painter, T.H., Thompson, D.R., 2022. Error and uncertainty degrade topographic corrections of remotely sensed data. J. Geophys. Res. Biogeosci. 127 https://doi.org/10.1029/2022JG007147.

Enderlin, E.M., Elkin, C.M., Gendreau, M., Marshall, H.P., O'Neel, S., McNeil, C., Florentine, C., Sass, L., 2022. Uncertainty of ICESat-2 ATL06- and ATL08-derived snow depths for glacierized and vegetated mountain regions. Remote Sens. Environ. 283, 113307 https://doi.org/10.1016/j.rse.2022.113307.

Gafurov, A., Bárdossy, A., 2009. Cloud removal methodology from MODIS snow cover product. Hydrol. Earth Syst. Sci. 13, 1361–1373. https://doi.org/10.5194/hess-13-1361-2009.

Gascoin, S., Grizonnet, M., Bouchet, M., Salgues, G., Hagolle, O., 2019. Theia snow collection: high-resolution operational snow cover maps from Sentinel-2 and Landsat-8 data. Earth Syst. Sci. Data 11, 493–514. https://doi.org/10.5194/essd-11-493-2019.

Gascoin, S., Barrou Dumont, Z., Deschamps-Berger, C., Marti, F., Salgues, G., López-Moreno, J.I., Revuelto, J., Michon, T., Schattan, P., Hagolle, O., 2020. Estimating fractional snow cover in open terrain from Sentinel-2 using the normalized difference snow index. Remote Sens. 12, 2904. https://doi.org/10.3390/rs12182904.

Girona-Mata, M., Miles, E.S., Ragettli, S., Pellicciotti, F., 2019. High-resolution snowline delineation from Landsat imagery to infer snow cover controls in a Himalayan catchment. Water Resour. Res. 55, 6754–6772. https://doi.org/10.1029/2019WR024935.

Grünewald, T., Bühler, Y., Lehning, M., 2014. Elevation dependency of mountain snow depth. Cryosph 8, 2381–2394. https://doi.org/10.5194/tc-8-2381-2014.

Hall, D.K., Riggs, G.A., Salomonson, V.V., 1995. Development of methods for mapping global snow cover using moderate resolution imaging spectroradiometer data. Remote Sens. Environ. https://doi.org/10.1016/0034-4257(95)00137-P.

Hantel, M., Maurer, C., 2011. The median winter snowline in the Alps. Meteorol. Z. 20, 267–276. https://doi.org/10.1127/0941-2948/2011/0495.

Hao, S., Jiang, L., Shi, J., Wang, G., Liu, X., 2019. Assessment of MODIS-based fractional snow cover products over the Tibetan plateau. IEEE J. Sel. Top. Appl. Earth Obs. Remote Sens. 12, 533–548. https://doi.org/10.1109/JSTARS.2018.2879666.

Hao, X., Huang, G., Che, T., Ji, W., Sun, X., Zhao, Q., Zhao, H., Wang, J., Li, H., Yang, Q., 2021. The NIEER AVHRR snow cover extent product over China – a long-term daily snow record for regional climate research. Earth Syst. Sci. Data 13, 4711–4726. https://doi.org/10.5194/essd-13-4711-2021.

Härer, S., Bernhardt, M., Siebers, M., Schulz, K., 2018. On the need for a time- and location-dependent estimation of the NDSI threshold value for reducing existing uncertainties in snow cover maps at different scales. Cryosph 12, 1629–1642. https://doi.org/10.5194/tc-12-1629-2018.

Hedrick, A.R., Marks, D., Havens, S., Robertson, M., Johnson, M., Sandusky, M., Marshall, H.P., Kormos, P.R., Bormann, K.J., Painter, T.H., 2018. Direct insertion of NASA airborne snow observatory-derived snow depth time series into the iSnobal energy balance snow model. Water Resour. Res. 54, 8045–8063. https://doi.org/10.1029/2018WR023190.

Hu, Z., Dietz, A.J., Kuenzer, C., 2019. Deriving regional snow line dynamics during the ablation seasons 1984-2018 in European mountains. Remote Sens. 11, 1–21. https://doi.org/10.3390/rs11080950.

Huning, L.S., AghaKouchak, A., 2020. Global snow drought hot spots and characteristics. Proc. Natl. Acad. Sci. 117, 19753–19759. https://doi.org/10.1073/pnas.1915921117.

John, A., Cannistra, A.F., Yang, K., Tan, A., Shean, D., Hille Ris Lambers, J., Cristea, N., 2022. High-resolution snow-covered area mapping in Forested Mountain ecosystems using PlanetScope imagery. Remote Sens. 14, 1–24. https://doi.org/10.3390/rs14143409.

Kelsey, K.C., Pedersen, S.H., Leffler, A.J., Sexton, J.O., Feng, M., Welker, J.M., 2021. Winter snow and spring temperature have differential effects on vegetation phenology and productivity across Arctic plant communities. Glob. Chang. Biol. 27, 1572–1586. https://doi.org/10.1111/gcb.15505.

Klein, A.G., Hall, D.K., Riggs, G.A., 1998. Improving snow cover mapping in forests through the use of a canopy reflectance model. Hydrol. Process. 12, 1723–1744. https://doi.org/10.1002/(SICI)1099-1085(199808/09)12:10/11<1723::AID-HYP691>3.0.CO;2-2.

Koehler, J., Bauer, A., Dietz, A.J., Kuenzer, C., 2022. Towards forecasting future snow cover dynamics in the European Alps—the potential of long optical remote-sensing time series. Remote Sens. 14 https://doi.org/10.3390/rs14184461.

Kostadinov, T.S., Schumer, R., Hausner, M., Bormann, K.J., Gaffney, R., McGwire, K., Painter, T.H., Tyler, S., Harpold, A.A., 2019. Watershed-scale mapping of fractional snow cover under conifer forest canopy using lidar. Remote Sens. Environ. 222, 34–49. https://doi.org/10.1016/j.rse.2018.11.037.

Krajčí, P., Holko, L., Perdigão, R.A.P., Parajka, J., 2014. Estimation of regional snowline elevation (RSLE) from MODIS images for seasonally snow covered mountain basins. J. Hydrol. 519, 1769–1778. https://doi.org/10.1016/j.jhydrol.2014.08.064.

Lai, C.Y., Kingslake, J., Wearing, M.G., Chen, P.H.C., Gentine, P., Li, H., Spergel, J.J., van Wessem, J.M., 2020. Vulnerability of Antarctica's ice shelves to meltwater-driven fracture. Nature 584, 574–578. https://doi.org/10.1038/s41586-020-2627-8.

Lei, L., Zeng, Z., Zhang, B., 2012. Method for detecting snow lines from MODIS data and assessment of changes in the nianqingtanglha mountains of the Tibet plateau. IEEE J. Sel. Top. Appl. Earth Obs. Remote Sens. 5, 769–776. https://doi.org/10.1109/JSTARS.2012.2200654.

Li, X., Wang, N., Wu, Y., 2022. Automated glacier snow line altitude calculation method using Landsat series images in the Google earth engine platform. Remote Sens. 14 https://doi.org/10.3390/rs14102377.

Ma, Y., He, T., Li, A., Li, S., 2021. Evaluation and intercomparison of topographic correction methods based on landsat images and simulated data. Remote Sens. 13, 1–21. https://doi.org/10.3390/rs13204120.

Margulis, S.A., Liu, Y., Baldo, E., 2019. A joint Landsat- and MODIS-based reanalysis approach for Midlatitude montane seasonal snow characterization. Front. Earth Sci. 7, 1–23. https://doi.org/10.3389/feart.2019.00272.

Minder, J.R., Durran, D.R., Roe, G.H., 2011. Mesoscale controls on the mountainside snow line. J. Atmos. Sci. 68, 2107–2127. https://doi.org/10.1175/JAS-D-10-05006.1.

Niittynen, P., Heikkinen, R.K., Luoto, M., 2018. Snow cover is a neglected driver of Arctic biodiversity loss. Nat. Clim. Chang. 8, 997–1001. https://doi.org/10.1038/s41558-018-0311-x.

Niittynen, P., Heikkinen, R.K., Luoto, M., 2020. Decreasing snow cover alters functional composition and diversity of Arctic tundra. Proc. Natl. Acad. Sci. 117, 21480–21487. https://doi.org/10.1073/pnas.2001254117.

Otsu, N., 1979. A threshold selection method from gray-level histograms. IEEE Trans. Syst. Man Cybern. 9, 62–66. https://doi.org/10.1109/TSMC.1979.4310076.

Painter, T.H., Deems, J.S., Belnap, J., Hamlet, A.F., Landry, C.C., Udall, B., 2010. Response of Colorado River runoff to dust radiative forcing in snow. Proc. Natl. Acad. Sci. 107, 17125–17130. https://doi.org/10.1073/pnas.0913139107.

Painter, T.H., Berisford, D.F., Boardman, J.W., Bormann, K.J., Deems, J.S., Gehrke, F., Hedrick, A., Joyce, M., Laidlaw, R., Marks, D., Mattmann, C., McGurk, B., Ramirez, P., Richardson, M., Skiles, S.M.K., Seidel, F.C., Winstral, A., 2016. The airborne snow observatory: fusion of scanning lidar, imaging spectrometer, and physically-based modeling for mapping snow water equivalent and snow albedo. Remote Sens. Environ. 184, 139–152. https://doi.org/10.1016/j.rse.2016.06.018.

Parajka, J., Pepe, M., Rampini, A., Rossi, S., Blöschl, G., 2010. A regional snow-line method for estimating snow cover from MODIS during cloud cover. J. Hydrol. 381, 203–212. https://doi.org/10.1016/j.jhydrol.2009.11.042.

Portenier, C., Hasler, M., Wunderle, S., 2022. Estimating regional snow line elevation using public webcam images. Remote Sens. 14, 4730. https://doi.org/10.3390/rs14194730.

Qin, Y., Abatzoglou, J.T., Siebert, S., Huning, L.S., AghaKouchak, A., Mankin, J.S., Hong, C., Tong, D., Davis, S.J., Mueller, N.D., 2020. Agricultural risks from changing snowmelt. Nat. Clim. Chang. 10, 459–465. https://doi.org/10.1038/s41558-020-0746-8.

Qin, Y., Hong, C., Zhao, H., Siebert, S., Abatzoglou, J.T., Huning, L.S., Sloat, L.L., Park, S., Li, S., Munroe, D.K., Zhu, T., Davis, S.J., Mueller, N.D., 2022. Snowmelt risk telecouplings for irrigated agriculture. Nat. Clim. Chang. 12, 1007–1015. https://doi.org/10.1038/s41558-022-01509-z.

Qiu, S., Zhu, Z., He, B., 2019. Fmask 4.0: improved cloud and cloud shadow detection in Landsats 4–8 and Sentinel-2 imagery. Remote Sens. Environ. 231, 111205 https://doi.org/10.1016/j.rse.2019.05.024.

Racoviteanu, A.E., Rittger, K., Armstrong, R., 2019. An automated approach for estimating snowline altitudes in the Karakoram and eastern Himalaya from remote sensing. Front. Earth Sci. 7 https://doi.org/10.3389/feart.2019.00220.

Raleigh, M.S., Rittger, K., Moore, C.E., Henn, B., Lutz, J.A., Lundquist, J.D., 2013. Ground-based testing of MODIS fractional snow cover in subalpine meadows and forests of the Sierra Nevada. Remote Sens. Environ. 128, 44–57. https://doi.org/10.1016/j.rse.2012.09.016.

Ripper, E., Schwaizer, G., Nagler, T., Metsämäki, S., Törmä, M., Fernandes, R., Crawford, C.J., Painter, T., Rittger, K., 2019. Guidelines for the Generation of Snow Extent Products from High Resolution Optical Sensors – FINAL.

Rittger, K., Painter, T.H., Dozier, J., 2013. Assessment of methods for mapping snow cover from MODIS. Adv. Water Resour. 51, 367–380. https://doi.org/10.1016/j.advwatres.2012.03.002.

Rittger, K., Raleigh, M.S., Dozier, J., Hill, A.F., Lutz, J.A., Painter, T.H., 2020. Canopy adjustment and improved cloud detection for remotely sensed snow cover mapping. Water Resour. Res. 56, 1–20. https://doi.org/10.1029/2019WR024914.

Salomonson, V.V., Appel, I., 2004. Estimating fractional snow cover from MODIS using the normalized difference snow index. Remote Sens. Environ. https://doi.org/10.1016/j.rse.2003.10.016.

Shea, J.M., Menounos, B., Moore, R.D., Tennant, C., 2013. An approach to derive regional snow lines and glacier mass change from MODIS imagery, western North America. Cryosph 7, 667–680. https://doi.org/10.5194/tc-7-667-2013.

Stillinger, T., Rittger, K., Raleigh, M.S., Michell, A., Davis, R.E., Bair, E.H., 2023. Landsat, MODIS, and VIIRS snow cover mapping algorithm performance as validated by airborne lidar datasets. Cryosph 17, 567–590. https://doi.org/10.5194/tc-17-567-2023.

Takaku, J., Tadono, T., Tsutsui, K., 2014. Generation of high resolution global DSM from ALOS PRISM. Int. Arch. Photogramm. Remote. Sens. Spat. Inf. Sci. XL–4, 243–248. https://doi.org/10.5194/isprsarchives-XL-4-243-2014.

Tang, Z., Wang, J., Li, H., Liang, J., Li, C., Wang, X., 2014. Extraction and assessment of snowline altitude over the Tibetan plateau using MODIS fractional snow cover data (2001 to 2013). J. Appl. Remote. Sens. 8, 084689 https://doi.org/10.1117/1.jrs.8.084689.

Teillet, P.M., Guindon, B., Goodenough, D.G., 1982. On the slope-aspect correction of multispectral scanner data. Can. J. Remote. Sens. 8, 84–106. https://doi.org/10.1080/07038992.1982.10855028.

Thaler, E.A., Crumley, R.L., Bennett, K.E., 2023. Estimating snow cover from high-resolution satellite imagery by thresholding blue wavelengths. Remote Sens. Environ. 285, 113403 https://doi.org/10.1016/j.rse.2022.113403.

Wang, J., Tang, Z., Deng, G., Hu, G., You, Y., Zhao, Y., 2023. Landsat satellites observed dynamics of snowline altitude at the end of the melting season, Himalayas, 1991–2022. Remote Sens. 15, 2534. https://doi.org/10.3390/rs15102534.

Wang, X., Wang, T., Xu, J., Shen, Z., Yang, Y., Chen, A., Wang, S., Liang, E., Piao, S., 2022. Enhanced habitat loss of the Himalayan endemic flora driven by warming-forced upslope tree expansion. Nat. Ecol. Evol. 6, 890–899. https://doi.org/10.1038/s41559-022-01774-3.

Wei, C., Karger, D.N., Wilson, A.M., 2020. Spatial detection of alpine treeline ecotones in the Western United States. Remote Sens. Environ. 240, 111672 https://doi.org/10.1016/j.rse.2020.111672.

Wickham, J., Stehman, S.V., Sorenson, D.G., Gass, L., Dewitz, J.A., 2021. Thematic accuracy assessment of the NLCD 2016 land cover for the conterminous United States. Remote Sens. Environ. 257, 112357 https://doi.org/10.1016/j.rse.2021.112357.

Wu, X., Naegeli, K., Wunderle, S., 2020. Geometric accuracy assessment of coarse-resolution satellite datasets: a study based on AVHRR GAC data at the sub-pixel level. Earth Syst. Sci. Data 12, 539–553. https://doi.org/10.5194/essd-12-539-2020.

Wunderle, S., Droz, M., Kleindienst, H., 2002. Spatial and temporal analysis of the snow line in the alps based on NOAA-AVHRR data. Geogr. Helv. 57, 170–183. https://doi.org/10.5194/gh-57-170-2002.

Xiao, X., Zhang, T., Zhong, X., Shao, W., Li, X., 2018. Support vector regression snow-depth retrieval algorithm using passive microwave remote sensing data. Remote Sens. Environ. 210, 48–64. https://doi.org/10.1016/j.rse.2018.03.008.

Xiao, X., Zhang, T., Zhong, X., Li, X., 2020. Spatiotemporal variation of snow depth in the northern hemisphere from 1992 to 2016. Remote Sens. 12, 2728. https://doi.org/10.3390/rs12172728.

Xiao, X., Liang, S., He, T., Wu, D., Pei, C., Gong, J., 2021. Estimating fractional snow cover from passive microwave brightness temperature data using MODIS snow cover product over North America. Cryosph 15, 835–861. https://doi.org/10.5194/tc-15-835-2021.

Xiao, X., He, T., Liang, Shunlin, Liu, X., Ma, Y., Liang, Shuang, Chen, X., 2022. Estimating fractional snow cover in vegetated environments using MODIS surface reflectance data. Int. J. Appl. Earth Obs. Geoinf. 114, 103030 https://doi.org/10.1016/j.jag.2022.103030.

Yin, D., Cao, X., Chen, X., Shao, Y., Chen, J., 2013. Comparison of automatic thresholding methods for snow-cover mapping using Landsat TM imagery. Int. J. Remote Sens. 34, 6529–6538. https://doi.org/10.1080/01431161.2013.803631.

Yin, H., Tan, B., Frantz, D., Radeloff, V.C., 2022. Integrated topographic corrections improve forest mapping using Landsat imagery. Int. J. Appl. Earth Obs. Geoinf. 108, 102716 https://doi.org/10.1016/j.jag.2022.102716.

Yu, F., Wang, P., Li, H., 2022. Surface albedo and snowline altitude estimation using optical satellite imagery and in situ measurements in Muz taw glacier, Sawir Mountains. Remote Sens. 14 https://doi.org/10.3390/rs14246405.

Zheng, Z., Kirchner, P.B., Bales, R.C., 2016. Topographic and vegetation effects on snow accumulation in the southern Sierra Nevada: a statistical summary from lidar data. Cryosphere 10, 257–269. https://doi.org/10.5194/tc-10-257-2016.

Zhong, X.Y., Zhang, T., Su, H., Xiao, X.X., Wang, S.F., Hu, Y.T., Wang, H.J., Zheng, L., Zhang, W., Xu, M., Wang, J., 2021. Impacts of landscape and climatic factors on snow cover in the Altai Mountains, China. Adv. Clim. Chang. Res. 12, 95–107. https://doi.org/10.1016/j.accre.2021.01.005.

Zhu, Z., Wang, S., Woodcock, C.E., 2015. Improvement and expansion of the Fmask algorithm: cloud, cloud shadow, and snow detection for Landsats 4–7, 8, and sentinel 2 images. Remote Sens. Environ. 159, 269–277. https://doi.org/10.1016/j.rse.2014.12.014.